Revealing the Surface Structure of CdSe Nanocrystals by Dynamic Nuclear Polarization-Enhanced ^{77}Se and ^{113}Cd Solid-State NMR Spectroscopy.

Yunhua Chen,[1,2,†] Rick W. Dorn,[1,2,†] Michael P. Hanrahan,[1,2] Lin Wei,[2] Rafael Blome-Fernández,[2] Alan M. Medina-Gonzalez,[2] Marquix A. S. Adamson,[2] Anne H. Flintgruber,[1] Javier Vela[1,2]* and Aaron J. Rossini[1,2]*

[1]US Department of Energy, Ames Laboratory, Ames, IA, USA 50011.

[2]Department of Chemistry, Iowa State University, Ames, IA, USA 50011.

Corresponding Authors

*e-mail: arossini@iastate.edu

*e-mail: vela@iastate.edu

Table of content:

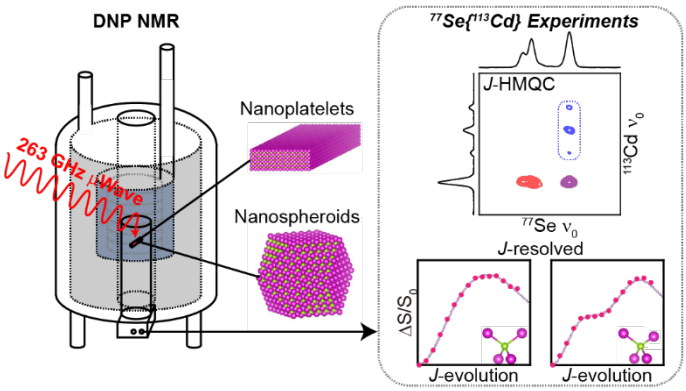

Abstract:

Dynamic nuclear polarization (DNP) solid-state NMR (SSNMR) spectroscopy was used to obtain detailed surface structures of zinc blende CdSe nanocrystals (NCs) with plate or spheroidal morphologies and which are capped by carboxylic acid ligands. 1D ^{113}Cd and ^{77}Se cross-polarization magic angle spinning (CPMAS) NMR spectra revealed distinct signals from Cd and Se atoms on the surface of the NCs, and those residing in bulk-like environments below the surface. ^{113}Cd cross-polarization magic-angle-turning (CP-MAT) experiments identified $CdSe_3O$, $CdSe_2O_2$, and $CdSeO_3$ Cd coordination environments on the surface of the NCs, where the oxygen atoms are presumably from coordinated carboxylate ligands. The sensitivity gain from DNP enabled natural isotopic abundance 2D homonuclear ^{113}Cd-^{113}Cd and ^{77}Se-^{77}Se and heteronuclear ^{113}Cd-^{77}Se scalar correlation solid-state NMR experiments that reveal the connectivity of the Cd and Se atoms. Importantly, ^{77}Se{^{113}Cd} scalar heteronuclear multiple quantum coherence (*J*-HMQC) experiments were used to selectively measure one-bond ^{77}Se-^{113}Cd scalar coupling constants (^{1}J(^{77}Se, ^{113}Cd)). With knowledge of

$^{1}J(^{77}Se, ^{113}Cd)$, heteronuclear $^{77}Se\{^{113}Cd\}$ spin echo (*J*-resolved) NMR experiments were then used to determine the number of Cd atoms bonded to Se atoms and vice versa. The *J*-resolved experiments directly confirmed that major Cd and Se surface species have $CdSe_2O_2$ and $SeCd_4$ stoichiometries, respectively. Considering the crystal structure of zinc blende CdSe, and the similarity of the solid-state NMR data for the platelets and spheroids, we conclude that the surface of the spheroidal CdSe NCs is primarily composed of {100} facets. The methods outlined here will generally be applicable to obtain detailed surface structures of various main group semiconductors.

Introduction:

Colloidal semiconductor NCs have generated significant attention as building block materials for optoelectronic and energy conversion devices,[1-7] as fluorophores for biological imaging,[8-10] and as photocatalysts.[11] Inorganic NCs usually consist of an ordered crystalline core and surface atoms that are typically passivated by organic ligands to impart colloidal stability.[12-14] The use of small inorganic ligands to passivate NCs is also well known.[14] The chemical, optical, and electronic properties of NCs can be conveniently tuned by modifying the composition,[15, 16] size/morphology,[17-19] and surface ligands.[20, 21] Due to their typical sizes of a few nanometers, a large fraction of each nanocrystal is made up of surface atoms. Consequently, the structure of the surface atoms strongly impacts the properties of NCs. For example, under-coordinated surface atoms cause localized electronic states that shorten exciton lifetimes and reduce photoluminescence quantum yields (PLQY).[22]

Unfortunately, the disordered and irregular nature of NC surfaces makes them challenging to study experimentally.[23] Typical NC characterization techniques such as electron microscopy and X-ray or electron diffraction primarily probe bulk structure. ^{1}H, ^{13}C, ^{19}F, and ^{31}P solution and solid-state nuclear magnetic resonance (SSNMR) and infrared spectroscopies provide detailed structural information about the organic ligands and have provided indirect evidence for the heterogeneity of NC surfaces,[24-32] but usually they do not directly probe the NC surface atoms. DFT calculations have become one of the primary tools to predict structures of surface atoms, ligand binding modes and linking these to NC optoelectronic properties.[32-39]

Many of the elements that make up the most investigated inorganic NCs have NMR-active isotopes. Consequently, magic angle spinning (MAS) solid-state NMR spectroscopy has found increasing applications in the study of both the bulk (interior) and surface structures of NCs. Direct excitation solid-state NMR spectra of the nuclei found in inorganic NCs (i.e., ^{29}Si, ^{31}P, ^{77}Se, ^{113}Cd, ^{123}Te, ^{133}Cs, ^{207}Pb, etc.) often show narrow NMR signals from atoms residing in their core, while broadened and shifted NMR signals attributed to surface atoms may be observed for smaller diameter particles.[40-47] Surface-selective solid-state NMR spectra may be obtained using CPMAS or other pulse schemes to selectively observe NMR signals from surface atoms that are coupled to the ^{1}H spins of surface ligands.[25, 43, 45, 48-59] For example, surface-selective ^{1}H→^{77}Se CP and CP-heteronuclear correlation (CP-HETCOR) experiments on CdSe NCs showed unique surface ^{77}Se chemical shifts, which were distinct from those observed in NMR experiments that probe the core Se atoms, thus suggesting that

the surface Se atoms have different structures and chemical environments from those of the bulk, possibly due to surface reconstruction.[43, 49] Similar experiments have also been performed on other NC systems.[25, 45, 46, 48, 50-59]

Conventional solid-state NMR spectroscopy suffers from poor sensitivity, resulting in long experiment times, restricting the types of experiments and structural information that it can provide.[49] High-field MAS dynamic nuclear polarization (DNP) has been shown to significantly enhance the sensitivity of solid-state NMR experiments by transferring polarization from unpaired electron spins of polarizing agents to nuclear spins at cryogenic temperatures.[60, 61] Currently, MAS DNP experiments on semiconductor NCs are performed by using inert support material, such as mesoporous silica, gels, or hexagonal boron nitride (*h*-BN), to disperse the NCs or minimize the size of the NC aggregates and maintain the proximity between the NC and the DNP polarizing agents after freezing the sample.[56, 57, 59, 62, 63] In this way, DNP enables many solid-state NMR experiments on semiconductor NCs such as HETCOR experiments with challenging natural isotopic abundance combinations (^{13}C-^{111}Cd, ^{13}C-^{29}Si, and ^{31}P-^{113}Cd), ^{113}Cd anisotropic chemical shift - isotropic chemical shift correlations (^{113}Cd-^{113}Cd), and through-bond and through-space homonuclear double-quantum single-quantum (DQ-SQ) correlation experiments (^{29}Si, ^{31}P or ^{113}Cd).[56, 57, 59, 62] Notably, DNP-enhanced surface-selective ^{111}Cd and ^{113}Cd SSNMR experiments have been performed on carboxylate capped CdS or CdSe NCs.[56, 57, 59, 62] The isotropic and anisotropic Cd chemical shifts suggest that most surface Cd atoms are coordinated by two surface chalcogen atoms and two oxygen atoms from carboxylate ligands (CdX_2O_2), [56, 57, 59, 62]

in agreement with accepted schemes describing NC surface chemistry.[13]

Here, we use DNP-enhanced ^{77}Se and ^{113}Cd SSNMR to obtain a molecular picture of the surface structures of carboxylate terminated CdSe NCs with nanoplatelet and nanospheroidal morphologies. 2D ^{113}Cd-^{113}Cd CP-MAT experiments show signatures for different Cd surface species. ^{113}Cd and ^{77}Se scalar homonuclear DQ-SQ correlation experiments reveal the connectivity between the surface and core Cd and Se atoms. Importantly, ^{77}Se{^{113}Cd} *J*-HMQC experiments illustrate Se-Cd linkages between core and surface atoms and enable selective measurement of Se-Cd one-bond scalar couplings (^{1}J(^{77}Se, ^{113}Cd)). With knowledge of ^{1}J(^{77}Se, ^{113}Cd), ^{77}Se{^{113}Cd} and ^{113}Cd{^{77}Se} heteronuclear spin echo (*J*-resolved) experiments can then be used to directly determine the number of Se or Cd atoms bonded to Cd and Se atoms ($SeCd_n$ and $CdSe_n$), respectively. Considering all of the information available from the DNP SSNMR experiments and other supporting techniques, such as FTIR spectroscopy and electron microscopy, we determine that the nanospheroids are primarily terminated with {100} surfaces capped with $CdSe_2O_2$ units, with less common {111} surfaces also present.

Results and discussion:

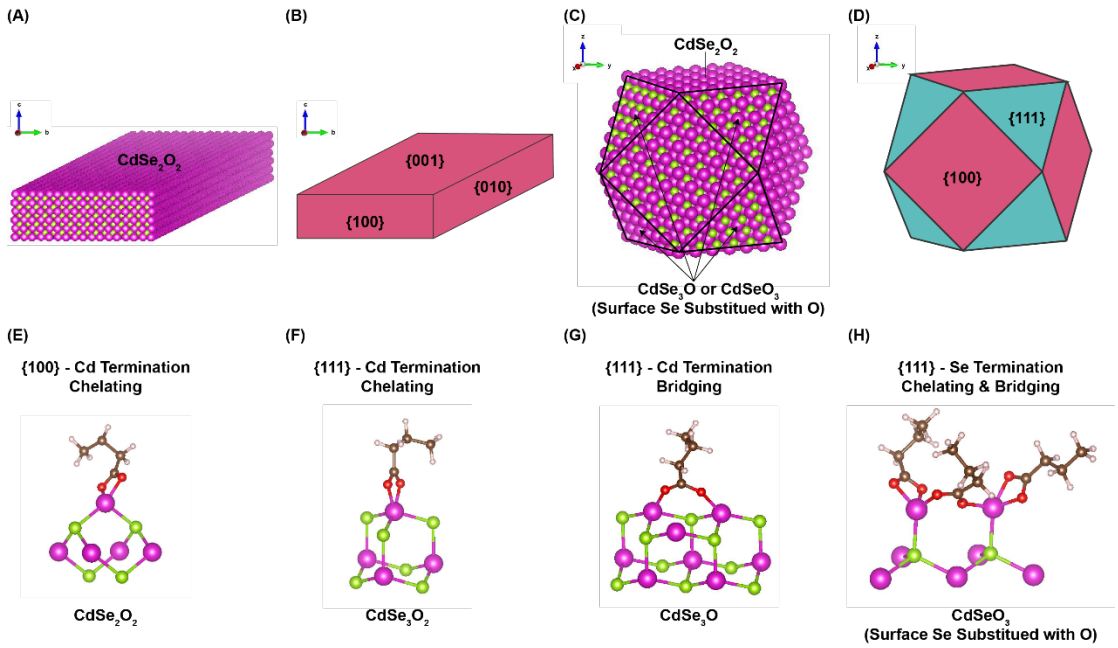

Figure 1. (A, C) Models of 8.4 nm × 26 nm × 1.71 nm CdSe nanoplatelets (A) and 3.5 nm CdSe nanospheroids (C). Corresponding surface Cd coordination on different facets is shown. (B, D) Models of CdSe nanoplatelets (B) and CdSe nanospheroids (D) with simplified illustrations of facets with the same orientation as (A) and (C). (E-H) Illustrations of possible coordination modes on the {100} (E) and {111} facets (F-H). Cd or Se termination, ligand binding modes (chelating or bridging), and surface Cd coordination are shown.

General Characterization and Surface Models. We prepared stearate/oleate capped zinc blende CdSe nanoplatelets and myristate/oleate capped CdSe nanospheroids using established methods (Figure 1, Figure 2 and Figure S1).[32, 64, 65] The proposed morphology of the different NCs derived from this study and prior studies is illustrated in Figure 1. Based on TEM images,[32, 66, 67] and considering their morphology, it is known that nanoplatelets are primarily terminated by {100} atomically flat basal planes.[32, 66-68]

On the other hand, there is less known about the surfaces of nanospheroids. Inductively coupled plasma optical emission spectroscopy (ICP OES) has revealed that

as-synthesized, carboxylate capped CdSe NCs usually have an excess amount of Cd because the surfaces are terminated by $Cd(O_2CR)_n$ units, where O_2CR is a carboxylate ligand.[69-71] Prior studies of platelet and spheroidal carboxylate capped CdSe NCs by DFT calculations, ^{13}C solid-state NMR and IR spectroscopies concluded that spherical NCs are primarily terminated by low-index facets from the {100} family and secondary {111} facets.[32] The {100} Cd surfaces were proposed to be capped by $CdSe_2O_2$ fragments, arising from bidentate chelating coordination of surface Cd by a carboxylate ligand (Figure 1E). In contrast, $CdSe_3O$ fragments arise on {111} facets because of bridging bidentate carboxylates (Figure 1G).[32] Other DFT and molecular dynamics studies of spheroidal NCs usually consider {100} and {111} facets with bridging and bidentate chelation.[23, 29, 36, 72] Prior DNP-enhanced ^{113}Cd solid-state NMR spectra have provided direct evidence for $CdSe_2O_2$ surface species.[32, 56, 57, 59] Hens and co-workers used quantitative ^{1}H solution NMR to measure oleic acid ligand densities of 5.4 nm^{-2} and 4.0 nm^{-2} for CdSe nanoplatelets[68] and 3.4 nm diameter nanospheroids,[29] respectively. Assuming the distance between the nearest neighbor Cd atoms on {100} surface matches that in the bulk lattice (4.39 Å), the carboxylate ligand density of the surface model shown in Figure 1 where a carboxylate chelates each Cd atom is 5.2 ligands nm^{-2}, in agreement with the previously reported experimental value for the nanoplatelets. This observation provides more evidence for the model of {100} surfaces shown in Figure 1.

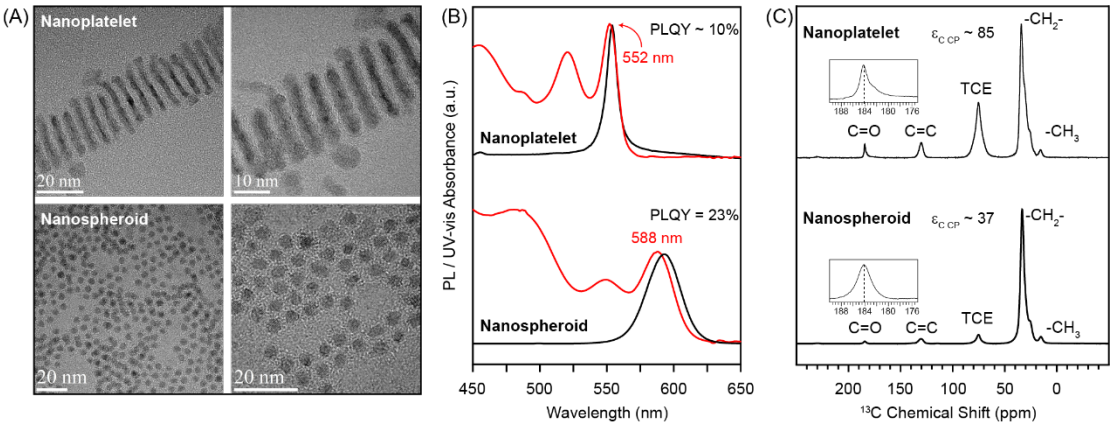

Figure 2. (A) TEM images, (B) UV-vis absorption (red lines) and PL (black lines) spectra, and (C) DNP-enhanced ^{13}C CPMAS NMR spectra of CdSe NCs in two different shapes: nanoplatelet and nanospheroid. The insets show the diagnostic high frequency chemical shifts of the carboxylate functional groups of surface ligands. The measured CPMAS DNP enhancement ($\varepsilon_{C\ CP}$) for the surface ligands was 85 for nanoplatelets and 37 for nanospheroids. The MAS rate was 10 kHz and the CP contact time was 2 ms.

Transmission electron microscopy (TEM) images of CdSe nanoplatelets illustrate the thickness of nanoplatelets studied here is 1.71 ± 0.40 nm (Figure 2A and Figure S2), which corresponds to 5.5 monolayer CdSe (6 layers of Cd and 5 layers of Se).[32] The average lateral dimensions of CdSe nanoplatelets are 8.4 nm × 26 nm. TEM images (Figure 2A and Figure S2) of spheroidal CdSe NCs show that they are monodisperse with a diameter of 3.6 ± 0.6 nm (Figure 2A and Figure S3). High-resolution TEM (HRTEM) images of nanoplatelets and nanospheroids show *d*-spacings of 3.40 Å and 2.16 Å corresponding to CdSe {111} and {022} planes, respectively (Figure S2). Ultraviolet-visible absorbance (UV-vis) and steady-state photoluminescence (PL) spectra of the CdSe nanoplatelets and nanospheroids confirm the particle sizes and sample morphologies (Figure 2B).[73]

DNP NMR experiments were performed on the nanoplatelets and nanospheroids

by adding anti-solvent to precipitate and purify the NCs, then physically mixing the precipitated NCs with *h*-BN, followed by impregnation with a TEKPol 1,1,2,2-tetrachloroethane solution.[62] DNP-enhanced ^{13}C CPMAS NMR spectra were acquired to extract DNP enhancements and identify and confirm the structure of the ligands on the CdSe NCs surfaces (Figure 2C). Comparison of ^{13}C CPMAS spectra obtained with and without microwave irradiation to drive DNP shows that the ^{13}C DNP enhancement was approximately 85 for nanoplatelets and 37 for nanospheroids, respectively. The high DNP enhancements enable challenging ^{77}Se-^{113}Cd NMR experiments, which provide a clear map of CdSe surface structures.

Since long-chain carboxylate ligands cap both CdSe nanoplatelets and nanospheroids, the ^{13}C solid-state NMR spectra are similar (Figure 2C). The most intense ^{13}C NMR signals cover a chemical shift range of ca. 10−40 ppm and correspond to carbons within the aliphatic alkyl chains of the ligands. The ^{13}C NMR signal at 75 ppm is attributed to 1,1,2,2-tetrachloroethane (TCE) from DNP sample preparation. The signal at 130 ppm is attributed to methylene carbons from oleate ligands. The lower intensity ^{13}C NMR signal at 184 ppm is attributed to carboxylate bound to the surface of the CdSe NCs. The carboxylate ^{13}C NMR signal of the CdSe nanospheroids is broader compared to that of the nanoplatelets, consistent with the findings of Kong and co-workers.[32] The ^{13}C solid-state NMR spectra show primarily chemical shifts of 184 ppm for both nanospheroids and nanoplatelets, indicating that the carboxylate groups primarily bind in a bidentate chelating manner to the surface Cd atoms on {100} surfaces.[32] Lower frequency ^{13}C carboxylate group chemical shifts at ca. 182 ppm are

attributed to bridging or tilted carboxylate ligands coordinated to Cd atoms on {111} or possibly {110} family of surfaces.[32] Given that the surfaces of the nanoplatelets are dominated by {100} facets, the shoulder peak at ca. 182 ppm for nanoplatelets should be associated with nanospheroids (seed) impurities (Figure S2), which are typical by-products during synthesis of nanoplatelets.[66, 74] The carboxylate binding mode assignments from ^{13}C solid-state NMR spectroscopy are validated by FTIR spectra (Figure S4 and S5).[32]

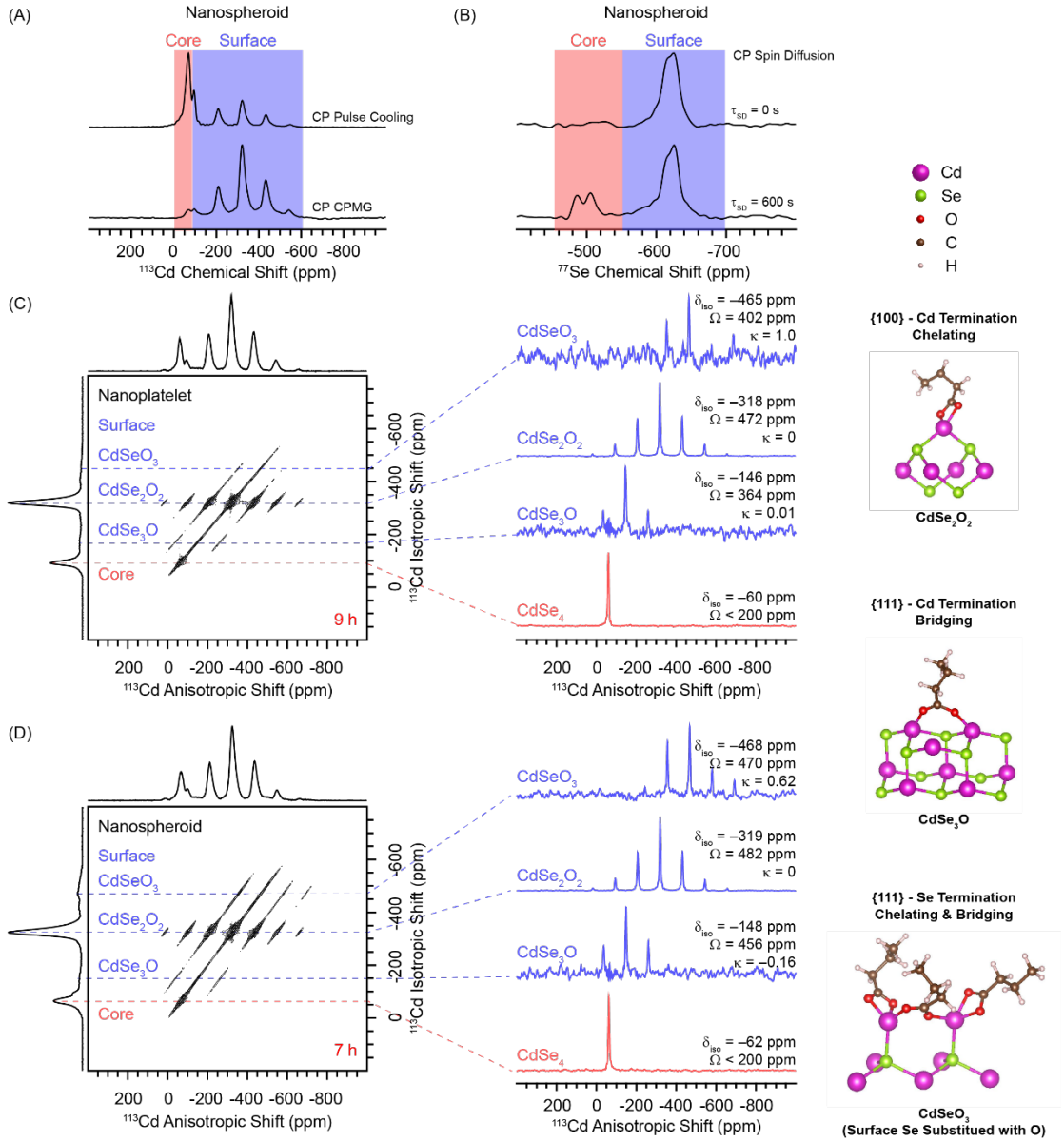

Figure 3. DNP-enhanced ^{113}Cd and ^{77}Se solid-state NMR spectra of CdSe NCs obtained with an MAS frequency of 10 kHz. (A) (Bottom) ^{113}Cd CP-CPMG and (top) CP pulse cooling spectra of CdSe nanospheroids. (B) ^{77}Se CP-CPMG spin diffusion spectra of CdSe nanospheroids with spin diffusion times of 0 and 600 s. (C, D) 2D ^{113}Cd CP-MAT spectra of CdSe nanoplatelets (C) and nanospheroids (D) where the dashed lines indicate distinct ^{113}Cd NMR signals. Individual rows extracted from the CP-MAT 2D spectrum showing ^{113}Cd sideband manifolds associated with isotropic core and surface NMR signals. The chemical shift tensor parameters are indicated.

Identification of Core and Surface ^{113}Cd and ^{77}Se NMR signals. DNP-enhanced ^{1}H→^{113}Cd CP Carr−Purcell−Meiboom−Gill (CPMG) and CP pulse cooling solid-state

NMR spectra were used to characterize the Cd environments within CdSe NCs (Figure 3A and pulse sequences are shown in Figure S6). The $^{1}H \rightarrow ^{113}Cd$ CP CPMG NMR spectrum shows several ^{113}Cd NMR signals attributed to core ($CdSe_4$ sites) and surface Cd ($CdSe_xO_{4-x}$ sites). The assignment of core and surface signals is further confirmed by DNP $^{1}H \rightarrow ^{113}Cd$ CP pulse cooling experiments. Pulse cooling uses a multiple-contact CP sequence to transport hyperpolarization to core ^{113}Cd spins via ^{113}Cd spin diffusion (Figure S6).[75] The proximity and ordering of the different Se sites were probed with ^{77}Se spin diffusion experiments, similar to pulse cooling.[62, 76] The ^{77}Se spin diffusion experiment clearly shows that the surface ^{77}Se magnetization is transferred to core sites by ^{77}Se spin diffusion (Figure 3B). It was previously demonstrated that CP contact times greater than 20 ms could directly transfer ^{1}H polarization to core ^{77}Se spins.[43, 49]

To further identify the different Cd coordination environments present in the CdSe NCs, 2D ^{113}Cd CP-MAT experiments were performed (Figure 3C and 3D).[59, 62, 77] The 2D CP-MAT spectrum correlates isotropic ^{113}Cd peaks, free of spinning sidebands in the indirect dimension, to spinning sideband manifolds that would be observed in a standard MAS NMR spectrum.[77] The isotropic ^{113}Cd chemical shifts observed in the indirect dimension of the 2D CP-MAT spectra provide clear information about the identity of the atoms coordinating Cd, while the sideband manifolds observed in the direct dimension allow determination of anisotropic chemical shift tensor parameters that report on the symmetry of the Cd atoms.[57, 59, 62] Interestingly, the 2D CP-MAT spectra of the platelets and spheroids are similar, with both showing four distinct isotropic ^{113}Cd NMR signals visible in the indirect dimension, although there are

differences in the relative signal intensities between the two samples and some slight differences in isotropic chemical shifts (Figure S7). The first signal occurs at an isotropic chemical shift of ca. −60 ppm, which matches the previously reported chemical shift for bulk CdSe.[49, 50, 56, 57, 59, 78] Therefore, this signal corresponds to $CdSe_4$ sites residing in the core or sub-surface regions of the CdSe NCs. As expected, this site has a small chemical shift anisotropy (CSA) (Ω < 200 ppm) consistent with the symmetric, tetrahedral arrangement of Se atoms. The other sites centered at ca. −146 ppm, −318 ppm, and −465 ppm are assigned to surface Cd atoms with $CdSe_3O$, $CdSe_2O_2$, $CdSeO_3$ coordination environments, respectively, where the oxygen atoms presumably come from carboxylate ligands, as discussed above. Surface ^{113}Cd NMR signals at −318 ppm have previously been assigned to CdX_2O_2 (X = S or Se) for CdS and CdSe NCs, including CdSe nanoplatelets.[43, 49, 56, 57, 59, 62] The isotropic chemical shifts assigned to $CdSe_3O$, $CdSe_2O_2$, $CdSeO_3$ sites are in good agreement with the relative differences in chemical shielding predicted by DFT calculations for $[Cd(SeH_2)_{4-n}(OH_2)_n]^{2+}$ (n = 0–4) molecular compounds.[59]

While the ^{113}Cd CPMAS and CP-MAT spectra are non-quantitative, the different surface species should have similar CP characteristics and signal intensities since the ^{1}H-^{113}Cd interatomic distance should be comparable for all Cd sites coordinated by a carboxylate ligand. The MAT spectra also indicate that all surface Cd sites possess similar CSA with a span greater than 350 ppm from the asymmetry of the surface Cd coordination environments (Figure 3C and 3D). Therefore, based upon the peak intensities in the MAT spectra of the nanospheroid and nanoplatelets, the $CdSe_2O_2$

fragment should be the most common on the surface and arise from {100} facets. $CdSeO_3$ and $CdSe_3O$ coordination environments should then arise from facets in the {111} family and possibly with some in the {110} family (Figure 1F, 1G, and 1H). The signals from {111} facets are of higher intensity in the CP-MAT spectrum of the nanospheroids because these other facets are needed to make a "curved" particle. In the nanoplatelets, the signals from {111} facets likely arise from defects, such as steps, corners, or edges, and from spheroid NC impurities (visible in TEM images, see Figure S2). In addition to the reduction in signals from {111} facets because of their limited area, the {111} signals will also be split between $CdSe_3O$ and $CdSeO_3$ fragments. Additional signal broadening would also be expected for signals arising from {111} facets because isotropic shift differences could arise for Cd atoms in the center versus edges of these smaller facets.

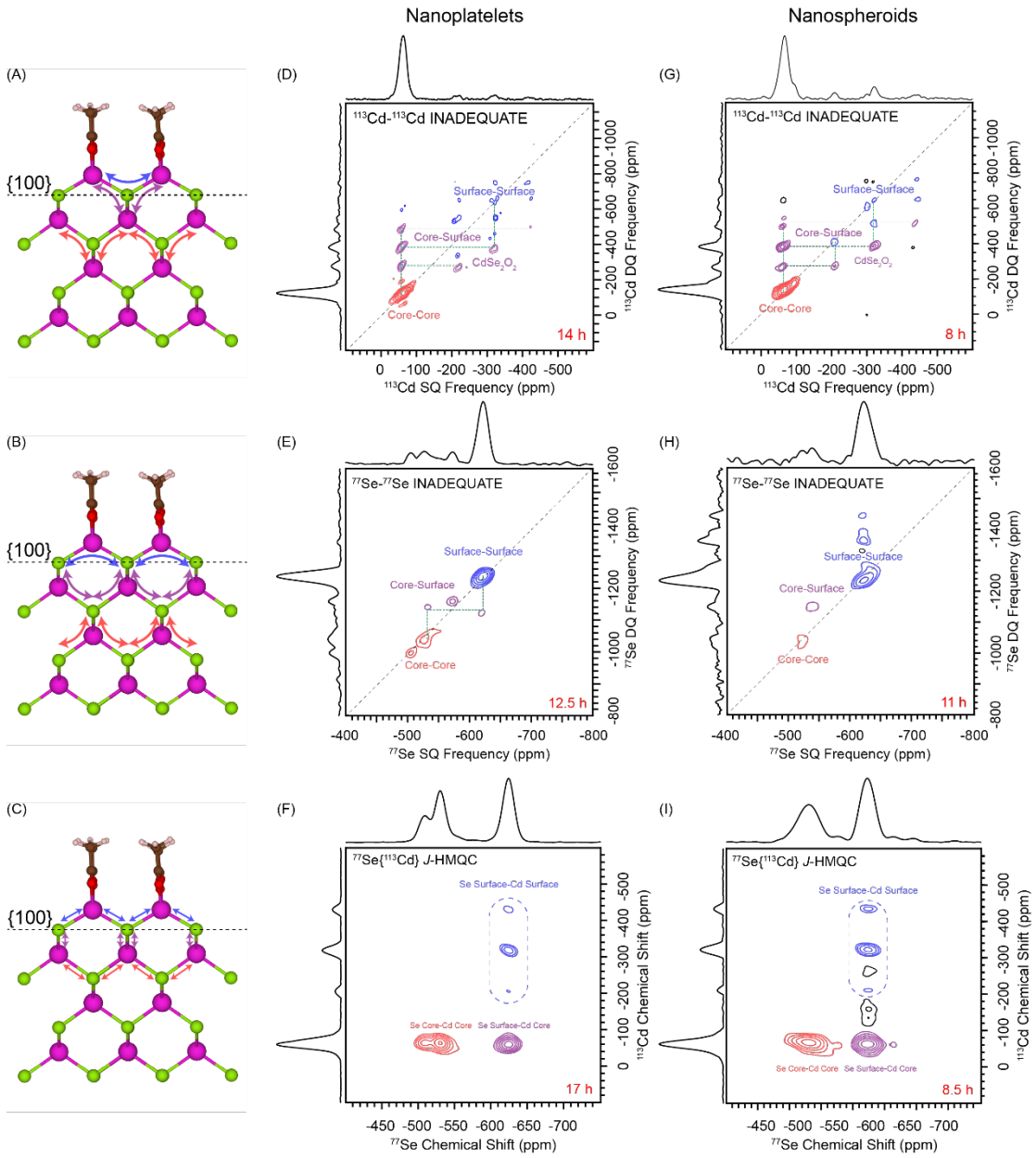

Figure 4. (A, B, C) Models of the surface of CdSe NCs derived from solid-state NMR spectroscopy. $Cd(O_2CMe)$ fragments are bonded to {100} Se surfaces. Each surface Cd atom has a $CdSe_2O_2$ coordination environment, while each surface Se atom has a $Se(Cd_{surface})_2(Cd_{core})_2$ coordination environment. Arrows illustrate connections between different Cd and Se atoms observed in the various 2D correlation spectra. (D, G) $^{113}Cd–^{113}Cd$ refocused-INADEQUATE spectra, (E, H) $^{77}Se–^{77}Se$ refocused-INADEQUATE spectra, and (F, I) $^{77}Se\{^{113}Cd\}$ constant time *J*-HMQC spectra of CdSe nanoplatelets and nanospheroids. Surface and core NMR signals are labeled on the NMR spectra. All spectra were recorded with DNP and a MAS frequency of 10 kHz and CPMG detection in t_2. Total experiment times are indicated.

Experiments. Having identified the different Cd coordination environments present in the CdSe NCs, homonuclear ^{113}Cd and ^{77}Se NMR experiments were used to confirm the connectivity of the different units and confirm structural models of the surface. The refocused incredible natural abundance double resonance transfer (refocused-INADEQUATE) experiment[79] was used to obtain homonuclear double-quantum single-quantum (DQ-SQ) correlation spectra. These spectra show NMR signals from homonuclear ^{113}Cd or ^{77}Se spin pairs linked (scalar coupled) by connecting Se or Cd atoms, respectively (Figure 4D, E, G, and H). The chemical shift in the indirect DQ dimension is determined by the sum of the SQ chemical shifts of the two *J*-coupled spins. These experiments are challenging because the natural isotopic abundance of ^{113}Cd and ^{77}Se is only 12.2% and 7.6%, respectively, leading to a low probability of having homonuclear spin pairs and low sensitivity; these experiments likely could not be performed without DNP. Inspection of Figure 4 shows the similarity of all 2D correlation spectra for the nanoplatelets and nanospheroids, immediately illustrating that the two morphologically different materials' surface structures must be similar.

The 2D ^{113}Cd–^{113}Cd refocused-INADEQUATE spectra obtained with a *J* evolution time (τ) of 2 ms gave optimal ^{113}Cd INADEQUATE NMR signal for the CdSe core, indicating the two-bond homonuclear cadmium *J* coupling ($^{2}J_{\mathrm{Cd-Cd}}$) is approximately 125 Hz (Figure S8). The 2D ^{113}Cd–^{113}Cd refocused-INADEQUATE spectrum shows a clear autocorrelation at −60 ppm in the direct dimension and −120 ppm in the indirect dimension, which corresponds to correlations between Cd core spins of CdSe NCs (as shown in red contour lines of Figures 4D and 4G). Correlations between core and

surface $CdSe_2O_2$ atoms result in off-diagonal intensities, confirming the connectivity of the core and surface Cd atoms (as shown in purple contour lines of Figures 4D and 4G). The $^{113}Cd–^{113}Cd$ 2D refocused-INADEQUATE spectrum also shows clear autocorrelations between Cd surface spins, providing direct evidence for the surface $CdSe_2O_2–CdSe_2O_2$ connections (as shown in blue contour lines of Figures 4D and 4G). Unfortunately, due to the low sensitivity of the $^{113}Cd–^{113}Cd$ 2D refocused-INADEQUATE experiments and their low signal intensity, ^{113}Cd NMR signals for $CdSe_3O$ and $CdSeO_3$ are not visible.

To elucidate the connectivity of Se species, 2D $^{77}Se–^{77}Se$ refocused-INADEQUATE experiments were performed. A τ value of 6 ms gave optimal ^{77}Se INADEQUATE NMR signal for the core $SeCd_4$ signals, which corresponds to a $^{2}J_{Se–Se}$ of approximately 40 Hz (Figure S9). The $^{77}Se–^{77}Se$ 2D INADEQUATE spectrum shows a weak autocorrelation at ca. −510 ppm in the direct dimension and ca. −1020 ppm in the indirect dimension from autocorrelations of core Se spins. Correlations between core and subsurface/surface Se atoms are also clearly observable, confirming that the surface and core Se atoms are connected by bridging Cd atoms. Intense surface Se autocorrelations are observed at ca. −625 ppm in the direct dimension and ca. −1250 ppm in the indirect dimension.

The connectivity between different Cd and Se chemical environments was determined with $^{77}Se\{^{113}Cd\}$ constant-time 2D scalar heteronuclear multiple quantum correlation (*J*-HMQC) experiments.[80-83] At 9.4 T ^{113}Cd and ^{77}Se possess similar resonance frequencies of 88.77 MHz and 76.29 MHz, respectively. The NMR probe's

X channel was simultaneously tuned to ^{113}Cd and ^{77}Se by using a REDOR box RF splitter (Figure S10).[84-86] In the ^{77}Se{^{113}Cd} *J*-HMQC experiments, ^{77}Se is first polarized by CP with an optimal 9 ms contact pulse, and CPMG detection is used to maximize sensitivity (Figure S6). The *J*-evolution time (τ) in the *J*-HMQC experiments was set to 5 ms, which corresponds to $^{1}J(^{77}\mathrm{Se},^{113}\mathrm{Cd})$ of approximately 100 Hz. The 2D ^{77}Se{^{113}Cd} *J*-HMQC spectra were obtained with 7.25 μs (34 kHz RF field) ^{113}Cd π/2 pulses to simultaneously excite both surface and core ^{113}Cd NMR signals. As expected, 2D ^{77}Se{^{113}Cd} *J*-HMQC spectra show a correlation between the core ^{77}Se NMR signal at –525 ppm and the core ^{113}Cd NMR signal at –60 ppm. The correlation at –625 ppm ^{77}Se chemical shift and –60 ppm ^{113}Cd chemical shift corresponds to surface Se-core Cd connections. The remaining correlation at –625 ppm ^{77}Se chemical shift and –318 ppm ^{113}Cd chemical shift should correspond to surface Se-surface Cd sites. Consistent with the models shown in Figure 4A-4C, core Se-surface Cd correlations are absent. Therefore, the *J*-HMQC spectrum confirms the signal assignments and the proposed CdSe NC structural models featuring Cd terminated surfaces.

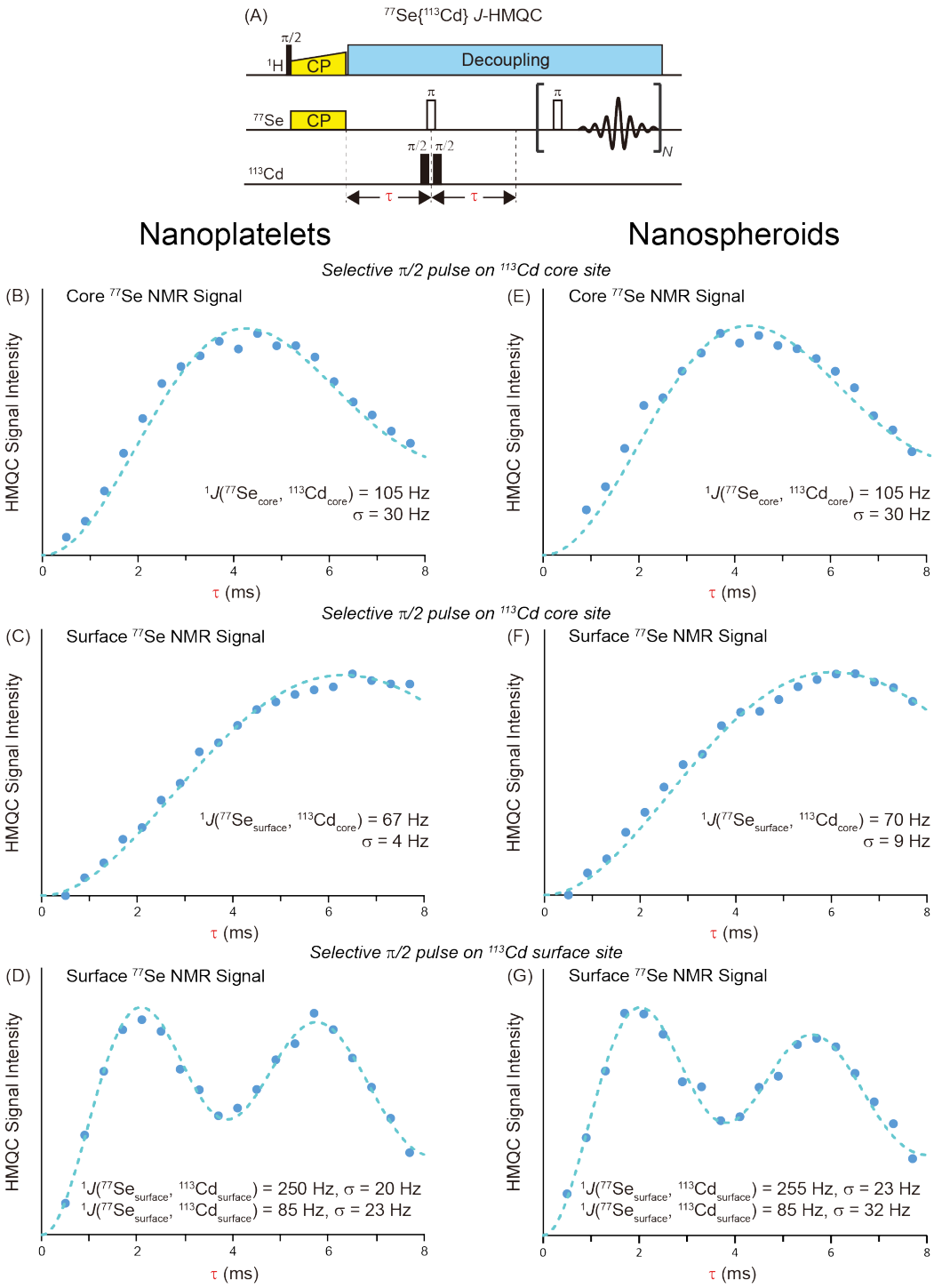

Figure 5. (A) ^{77}Se{^{113}Cd} *J*-HMQC pulse program with variable ^{77}Se-^{113}Cd *J*-evolution periods (τ) and ^{77}Se CPMG signal detection. The ^{113}Cd π/2 pulses were 100 μs in duration (2.5 kHz RF field) to allow selective excitation of surface or core Cd signals. (B−G) ^{77}Se{^{113}Cd} *J*-HMQC signal intensity as a function of τ for (B-D) CdSe nanoplatelets (B−D) and nanospheroids (E−G). (B, E) Selective π/2 pulses on ^{113}Cd core site, monitoring ^{77}Se core signal intensity. (C, F) Selective π/2 pulses on ^{113}Cd core site, monitoring ^{77}Se surface signal intensity. (D, G) Selective π/2 pulses on ^{113}Cd surface site, monitoring ^{77}Se surface signal intensity. The green dashed lines are the best fit. The best-fit *J*-couplings are indicated on the plots.

Determination of Cd-Se J-couplings. The *J*-HMQC experiments can also be used to measure the magnitude of $^{1}J(^{77}Se, ^{113}Cd)$ by varying the evolution time (τ) in the *J*-HMQC experiment (Figure 5A). Selective ^{113}Cd π/2 pulses 100 μs in duration (2.5 kHz RF field) were applied on resonance with either core or surface ^{113}Cd NMR signals to selectively measure $^{1}J(^{77}Se, ^{113}Cd)$ for the three different types of Se-Cd bonds (Figure S11). The dependence of the $^{77}Se\{^{113}Cd\}$ *J*-HMQC signal intensity (I_{HMQC}) on τ was fit with the following analytical equation:

$$I_{HMQC} = \exp\left(-2\tau/T_2'\right)\sum_{J_n=1\,Hz}^{J_n=500\,Hz}\frac{c}{\sigma\sqrt{2\pi}}exp\left(-\frac{1}{2}\frac{(J_n-J)}{\sigma}\right)sin^2(\pi J_n\tau) \quad (1)$$

Where T_2' is ^{77}Se homogenous transverse relaxation time, *c* is an arbitrary intensity scaling factor, σ gives the width of the Gaussian distribution of *J*-coupling values, and *J* is the central value of $^{1}J(^{77}Se, ^{113}Cd)$ in the distribution. A Gaussian distribution of *J*-couplings was considered because of the intrinsically disordered nature of NCs, although reasonable fits can be obtained if only a single value of $^{1}J(^{77}Se, ^{113}Cd)$ is considered (Figure S12). During the fitting, the value of T_2' was fixed at 20 ms for surface Se NMR signals based upon independent $^{1}H\rightarrow^{77}Se$ CP CPMG experiments and subsequent fitting of *J*-resolved curves (Figure S13).

For both nanoplatelets and nanospheroids, the best fit value for $^{1}J(^{77}Se_{core}, ^{113}Cd_{core})$ was 105 Hz with an identical distribution width (σ = 30 Hz, Figures 5B and 5E). When applying selective π/2 pulses on ^{113}Cd core sites, the surface ^{77}Se signals build up slightly slower than that of the core ^{77}Se signal. Fits of this curve yield $^{1}J(^{77}Se_{surface}, ^{113}Cd_{core})$ = 67 or 70 Hz with σ = 4 or 9 Hz. Interestingly, when the selective π/2 pulses are applied to ^{113}Cd surface signals, the surface $^{77}Se\{^{113}Cd\}$ *J*-HMQC signal shows a

much faster build-up with a "double-hump". These features can be fit with two values of $^{1}J(^{77}Se_{surface}, ^{113}Cd_{surface})$, which are 250 or 255 Hz (σ = 20 or 23 Hz) and 85 Hz (σ = 23 or 32 Hz). The observation of $^{1}J(^{77}Se_{surface}, ^{113}Cd_{surface})$ being much larger than $^{1}J(^{77}Se_{core}, ^{113}Cd_{core})$ is surprising. $^{1}J(^{77}Se_{surface}, ^{113}Cd_{surface})$ could be larger because a carboxylate ligand is a weaker electron donor to Cd than the softer Se atoms, resulting in a stronger Cd-Se bond for one of the surface Se atoms. The observation of two disparate values of $^{1}J(^{77}Se_{surface}, ^{113}Cd_{surface})$ could reflect a distortion of the {100} surfaces brought about by surface reconstruction. In this scenario, one of the Cd-Se bonds would be shorter than the other to explain the large increase in *J*-coupling. We note that the $^{77}Se\{^{113}Cd\}$ heteronuclear spin echo experiments confirm the values of $^{1}J(^{77}Se, ^{113}Cd)$ measured by *J*-HMQC (see below). The measured values of *J*-couplings are in line with $^{1}J(^{77}Se, ^{113}Cd)$ previously reported in the literature.[87-89] $^{1}J(^{77}Se, ^{113}Cd)$ of 120 Hz and 135 Hz was reported for dichalcogenoimidodiphosphinato complexes that feature Cd-Se bonds,[87] 250 Hz to 330 Hz was reported for $[Et_4N]_2[Cd(Se_4)_2]$,[88] and $^{1}J_{Se\text{-}Cd}$ linearly varied from 126 Hz (n = 0) to 46 Hz (n = 3) in the compounds $K_2[Cd(SPh)_n(SePh)_{4-n}]$.[89]

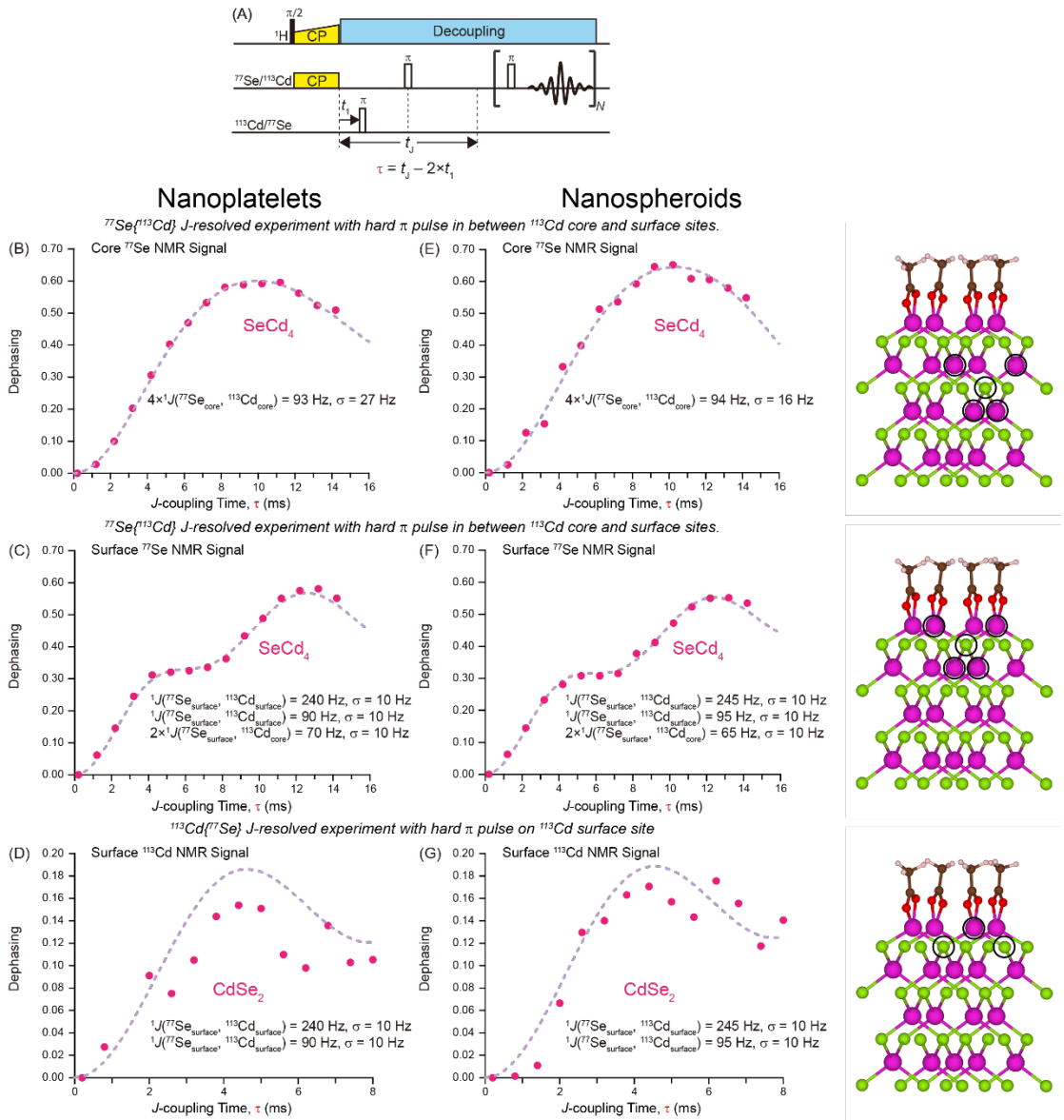

Figure 6. (A) ^{77}Se{^{113}Cd}/^{113}Cd{^{77}Se} constant-time *J*-resolved pulse sequence. (B–G) Dependence of the ^{77}Se signal dephasing on the *J*-coupling evolution time (τ) for CdSe nanoplatelets (B–D) and nanospheroids (E–G) in ^{77}Se{^{113}Cd}/^{113}Cd{^{77}Se} *J*-resolved experiments (pink dots). (B, E) ^{77}Se{^{113}Cd} *J*-resolved experiments with a hard π pulse in between ^{113}Cd core and surface sites, monitoring ^{77}Se core signal dephasing. (C, F) ^{77}Se{^{113}Cd} *J*-resolved experiments with a hard π pulse in between ^{113}Cd core and surface sites, monitoring ^{77}Se surface signal dephasing. (D, G) ^{113}Cd{^{77}Se} *J*-resolved experiments with a hard π pulse on ^{113}Cd surface sites, monitoring ^{113}Cd surface signal dephasing. The purple dashed lines are the best fit. The best-fit *J*-couplings are indicated on the plots. The structures on the right highlight the atoms probed in each experiment.

Determination of Cd and Se Stoichiometries with J-Resolved Experiments. With knowledge of ^{1}J(^{77}Se, ^{113}Cd) from the *J*-HMQC τ variation experiments, ^{77}Se{^{113}Cd}

heteronuclear spin-echo (*J*-resolved) experiments[82, 90, 91] were then used to directly determine the number of Cd atoms attached to each Se atom ($SeCd_n$). The application of π pulses on both ^{77}Se and ^{113}Cd channels in the *J*-resolved block causes the evolution of ^{77}Se-^{113}Cd *J* couplings and signal dephasing, with the dephasing maximized when $\tau = 1/J$ (for a single value of $^1J(^{77}Se, ^{113}Cd)$). Due to the 12.2% natural abundance of the ^{113}Cd isotope, the extent of dephasing observed in a $^{77}Se\{^{113}Cd\}$ *J*-resolved NMR signal for a $SeCd_n$ unit depends upon the number of bonded Cd atoms (Figure S14). For example, for a tetrahedral $SeCd_4$ site, the probabilities of having isotopomers with 0, 1, 2, 3, and 4 attached ^{113}Cd spins is $p_0 = 0.593$, $p_1 = 0.331$, $p_2 = 0.069$, $p_3 = 0.0064$ and $p_4 = 0.0002$, respectively (Figure S14). These calculations can be repeated for any $SeCd_n$ units with $n = 1$, 2, or 3 and used to predict the dephasing (Figure S14). Equation 2 relates the dephasing observed to the probability of each isotopomer (p_n) occurring:

$$Dephasing = 1 - f\left(\sum_{n=0}^{n=4}\sum_{J_m=1\,Hz}^{J_m=500\,Hz}\frac{c}{\sigma\sqrt{2\pi}}exp\left(-\frac{1}{2}\frac{(J_m-J)}{\sigma}\right)p_n\cos^n\left(\pi J_m\tau_J\right)]\right) \quad (2)$$

Theoretically, the maximum dephasing for SeCd, $SeCd_2$, $SeCd_3$, and $SeCd_4$ should be 0.24, 0.43, 0.57, and 0.67, assuming that all $^1J(^{77}Se, ^{113}Cd)$ are the same (Figure S14). The maximum dephasing is around 0.60 for the core ^{77}Se signal, which corresponds to $SeCd_4$ coordination after accounting for the reduction in dephasing brought about by a distribution in $^1J(^{77}Se, ^{113}Cd)$ (see below). The *J*-resolved curves for the core ^{77}Se NMR signals of both CdSe NCs can be fit using equation 2 with $^1J(^{77}Se_{core}, ^{113}Cd_{core}) = 93$ Hz and $\sigma = 27$ Hz for CdSe nanoplatelets and $^1J(^{77}Se_{core}, ^{113}Cd_{core}) = 94$ Hz and $\sigma = 16$ Hz for CdSe nanospheroids, consistent with the values of $^1J(^{77}Se, ^{113}Cd)$ determined by *J*-HMQC experiments.

When monitoring the surface ^{77}Se NMR signal in the *J*-resolved experiment, the maximum dephasing is only around 0.57, suggesting $SeCd_3$ coordination (Figure 6C, 6F, and Figure S15). However, two mechanisms reduce the experimental dephasing. First, the RF splitter used for the ^{77}Se-^{113}Cd double resonance experiments limits the maximum achievable ^{113}Cd RF field to 34 kHz (corresponding to a 14.5 μs π-pulse). SIMPSON[92] numerical simulations of *J*-resolved experiments show that if the offset of the 14.5 μs π pulse is placed in between ^{113}Cd core and surface sites, then the ^{113}Cd surface signals are inverted with only 77% efficiency because they have a significant CSA. The imperfect inversion is accounted for with the dephasing factor $f_{surface} = 0.77$ in equation 2. Recall, the 2D ^{77}Se{^{113}Cd} *J*-HMQC clearly shows that there must be scalar couplings between the surface Se atoms and at least one surface Cd atom. Second, the *J*-HMQC experiments indicate that $^{1}J(^{77}Se_{surface}, ^{113}Cd_{core})$ and $^{1}J(^{77}Se_{surface}, ^{113}Cd_{surface})$ values are different. The differences in surface and core *J*-couplings (and the distribution within each of these values) will result in only partial constructive interference and less dephasing. Hence, taking the mechanisms that reduce the *J*-dephasing into account, the surface Se atoms must have $SeCd_4$ coordination (Figures 6C, 6F, and S16). Indeed, the *J*-resolved curves can be fit using the values of $^{1}J(^{77}Se_{surface}, ^{113}Cd_{surface})$, $^{1}J(^{77}Se_{surface}, ^{113}Cd_{core})$, and σ similar to those determined with *J*-HMQC experiments (with equation 2 modified to take the different values of $^{1}J(^{77}Se, ^{113}Cd)$ for core and surface bonds into account, see Supporting Information). The *J*-resolved curves confirm $^{1}J(^{77}Se_{surface}, ^{113}Cd_{core})$ is around 70 Hz in both CdSe NCs and that there are two distinct values of ca. 240 Hz and ca. 90 Hz for $^{1}J(^{77}Se_{surface},$

$^{113}Cd_{surface}$).

Finally, to verify that the primary surface Cd atoms have $CdSe_2O_2$ coordination, $^{113}Cd\{^{77}Se\}$ *J*-resolved experiments were performed. $^{113}Cd\{^{77}Se\}$ dephasing is challenging to observe given the lower sensitivity of ^{113}Cd solid-state NMR and the 7.6% natural isotopic abundance of ^{77}Se. Regardless, for both types of CdSe NCs, the dephasing reaches a maximum of ca. 0.16, consistent with $CdSe_2$ coordination. The $^{113}Cd\{^{77}Se\}$ *J*-resolved curves can be reasonably fit by the values of $^{1}J(^{77}Se_{surface}, ^{113}Cd_{surface})$ of ca. 240 Hz and ca. 90 Hz obtained from the $^{77}Se\{^{113}Cd\}$ *J*-HMQC and *J*-resolved experiments.

Conclusions

1D and 2D homonuclear and heteronuclear ^{113}Cd and ^{77}Se correlation DNP NMR experiments reveal the connectivity of the different core and surface Cd and Se atoms within CdSe nanoplatelets and nanospheroids. Heteronuclear $^{77}Se\{^{113}Cd\}$ *J*-HMQC and *J*-resolved experiments disclose the number of Cd atoms attached to each Se atom. The primary Se surface species were determined to have $SeCd_4$ coordination, with bonds to two surface Cd atoms and two core Cd atoms ($SeCd_{2,core}Cd_{2,surface}$). Considering the similarity of all NMR data for the CdSe nanoplatelets and nanospheroids, and information from prior studies,[32] we can conclude that the surfaces of both types of NCs primarily consist of {100} Se surfaces [$Se(Cd_{core})_2(Cd_{surface})_2$ units], where the surface cadmium atoms consist of $Cd(Se_{surface})_2(O_2CR)$ units. The ^{113}Cd CP-MAT spectra suggest that in the nanospheroids, secondary Cd surface species

with $CdSe_3O$ and $CdSeO_3$ coordinations are also present and likely associated with the {111} family of facets. Unfortunately, NMR signals from the secondary {111} surfaces could not be observed in the homonuclear and heteronuclear correlation NMR experiments due to the combination of the breadth of their isotropic ^{113}Cd NMR signals, their large chemical shift anisotropies, their lower signal intensities, and their overlap with intense signals from the primary $CdSe_2O_2$ surface species.

Based on the results of this study, there are many interesting future directions of research. First, it should be possible to detect the minor surface facets and defects in 2D correlation NMR experiments by further enhancing NMR sensitivity. Sensitivity could be increased by combining fast MAS and DNP,[93] and potentially using ^{1}H detection, and/or performing DNP at lower temperatures with helium gas for sample cooling and spinning.[94, 95] Faster MAS frequencies would simplify the ^{113}Cd NMR spectra by reducing the intensity and number of spinning sidebands. Work along these lines is underway in our lab. Second, CdSe NCs with different morphologies, exposed surface facets, surface ligands, etc., can be studied to unravel the influence of surface structure on chemical and optoelectronic properties. Lastly, the solid-state NMR experiments demonstrated here should be applicable to other inorganic semiconductors NCs consisting of elements with spin-1/2 isotopes such as ^{29}Si, ^{31}P, ^{123}Te, ^{133}Cs, and ^{207}Pb.

Experimental Section

Synthesis.

Materials for synthesis. Cadmium acetate dihydrate ($Cd(OAc)_2 \cdot 2H_2O$, 98%), cadmium nitrate tetrahydrate ($Cd(NO_3)_2 \cdot 4H_2O$, 98%), 1-octadecene (ODE, 90%) and oleylamine ($OleyNH_2$, 70%) were purchased from Sigma-Aldrich; sodium hydroxide (NaOH, >97%), methanol (MeOH, HPLC grade), stearic acid (laboratory grade), hexanes (99.9%), chloroform ($CHCl_3$, certified ACS), toluene (certified ACS), and acetone (certified ACS) were from Fisher; tetramethylammonium hydroxide (98%), myristic acid (98%), and oleic acid (90%) were from Alfa Aesar; selenium powder (Se, 99.5%) and selenium dioxide (SeO_2, 99.8%) were from Strem. All chemicals were used as received.

Cadmium stearate.[96] Stearic acid (20 mmol, 5.689 g) and tetramethylammonium hydroxide (20 mmol, 1.823 g) were dissolved in MeOH (100 mL) by stirring for 20 min. $Cd(OAc)_2 \cdot 2H_2O$ (10 mmol, 2.665 g) was dissolved in MeOH (20 mL) and added into the mixture dropwise. A white precipitate formed while stirring for 20 minutes. The precipitate was separated by filtration and washed three times with MeOH. The precipitate was dried under vacuum for 6 hours.

CdSe nanoplatelets.[32] Cadmium stearate (0.30 mmol, 0.203 g) and ODE (9.468g, 12 mL) were degassed under a dynamic vacuum at room temperature for 10 minutes inside of a Schlenk flask. The flask was refilled with argon gas and heated to 240 °C. Se-ODE (2 mL, 0.1 M) was quickly injected. After 1 min, $Cd(OAc)_2 \cdot 2H_2O$ (0.45 mmol, 0.120 g) was suspended in ODE (0.789 g, 1 mL) and injected into the mixture. The

reaction was kept at 240 °C for 30 min. The mixture was cooled to 160 °C, and oleic acid (0.48 mmol, 0.15 mL) was swiftly injected to stop the reaction. After cooling to 80 °C, the final products were first isolated by centrifugation at 14000 rpm for 2 minutes. The supernatant was removed and the precipitate was then dissolved in toluene to form a clear solution, and was isolated by centrifugation at 10000 rpm for 2 minutes. The supernatant was removed for the second time and the dark red precipitate was dissolved in a mixture of chloroform, acetone, methanol, oleic acid, and oleylamine (volume ratio = 5:5:5:3:1), and the precipitate was isolated by centrifugation at 10000 rpm for 2 minutes. Decantation was performed to remove the supernatant. The last precipitation procedure was repeated twice. The CdSe nanoplatelets were then vacuum dried at room temperature for one hour.

Cadmium myristate.[97] Cadmium nitrate tetrahydrate (5.0 mmol, 1.542 g) was dissolved in MeOH (50 mL). A sodium myristate solution was prepared by dissolving NaOH (15 mmol, 0.599 g) and myristic acid (15 mmol, 3.425 g) in MeOH (500 mL). The $Cd(NO_3)_2$ solution was added dropwise (1 drop/s) into the sodium myristate solution with vigorous stirring. The resulting white precipitate was washed with methanol three times and then dried at 60 °C under vacuum overnight.

CdSe nanospheroids.[65, 97] SeO_2 (0.1 mmol, 0.011 g) and cadmium myristate (0.1 mmol, 0.056 g) were added to a three-neck flask with ODE (5.0 g, 6.34 mL). The mixture was degassed for 10 minutes under vacuum at room temperature. Under argon flow, the solution was stirred and heated to 240 °C at a rate of 25 °C/min. After reaching 240 °C, the sample was held at this temperature for 2 minutes, then 1 mL of oleic acid

was added dropwise into the reaction solution to stabilize the nanocrystals' growth. The reaction was maintained at 240 °C for an additional 30 min, and then the reaction mixture was cooled to room temperature by removing from the heat source. The resulting particles were precipitated by adding acetone, centrifugation (2 minutes at 14000 rpm), and then redispersed in toluene. The particles were further purified by precipitation-redispersion three more times.

Dynamic Nuclear Polarization Solid-State NMR Spectroscopy

DNP Sample Preparation. In general, 25 mg of powdered CdSe NCs (nanoplatelets or nanospheroids) and 25 mg of *h*-BN were weighed out and placed into a mortar. The two materials were gently ground for *ca.* 1 minute with a mortar and pestle to mix the CdSe NCs and *h*-BN support material. *ca.* 30 mg portion of the powder mixture was then placed in a watch glass, where 15 μL of a 16 mM TEKPol TCE solution was added and thoroughly mixed for the nanospheriods and nanoplatelets, respectively. The sample was then packed into a 3.2 mm (outer diameter) DNP sapphire rotor with a Teflon insert and zirconia drive cap.

General Experimental Details. All DNP experiments were performed on a Bruker 400 MHz/263 GHz NMR magnet/gyrotron equipped with a Bruker AVANCE III spectrometer console and a Bruker 3.2 mm HXY MAS DNP-NMR probe configured in double resonance mode. The sample temperature was *ca.* 100-110 K for all experiments. ^{1}H, ^{13}C, ^{77}Se and ^{113}Cd radio frequency (RF) pulses were directly calibrated on each sample either through a (^{1}H) single pulse or (^{13}C, ^{77}Se and ^{113}Cd) ^{1}H→X (X = ^{13}C, ^{77}Se or ^{113}Cd) CP-90 nutation experiment. ^{1}H→X (X = ^{13}C, ^{77}Se or

^{113}Cd) CP was performed at the beginning of all experiments to enhance sensitivity and selectively probe the surface of the NCs. All ^{1}H CP spin-lock RF fields were linearly ramped from 90% to 100% amplitude[98] to broaden to Hartman-Hahn match condition. The RF fields, CP duration and MAS frequencies for all experiments are given in Table S1. 100 kHz ^{1}H RF field SPINAL-64 heteronuclear decoupling[99] was applied during all evolution periods and during the acquisition ^{13}C, ^{77}Se or ^{113}Cd. ^{1}H chemical shifts were referenced to neat tetramethylsilane using frozen TCE (δ_{iso}(^{1}H) = 6.2 ppm) as a secondary chemical shift standard. Previously published relative NMR frequencies were used to indirectly reference the ^{13}C, ^{113}Cd, and ^{77}Se chemical shifts.[100] DNP-enhanced CP spin echo, CP-CPMG,[101] CP Pulse Cooling,[75] CP spin diffusion,[76] refocused-INADEQUATE-CPMG,[62, 79] heteronuclear *J*-resolved[81, 102] and *J*-HMQC experiments[83] were performed using previously described pulse sequences. A schematic illustration of all pulse sequences is shown in Figure S6. ^{113}Cd CP pulse cooling experiments were acquired with CPMG signal detection, a 7 s delay (τ_z) after each CP block and 15 CP cycles (L) to amplify bulk polarization.[75] Constant-time ^{113}Cd CP-MAT experiments were acquired using the five-π pulse MAT pulse sequence.[77] The ^{113}Cd chemical shift tensor parameters (δ_{iso}, Ω, κ, using the Herzfeld-Berger convention) were determined by extracting sideband manifolds from the isotropic (indirect) dimension of the 2D MAT spectra and fitting the manifold with the solid lineshape analysis (SOLA) module in the Bruker TopSpin 3.6.1 software. ^{113}Cd refocused-INADEQUATE-CPMG experiments were acquired with a 2 ms scalar coupling evolution time (τ_J), corresponding to 8 ms of total *J*-evolution.

^{77}Se spin diffusion NMR spectra were acquired with a selective rectangular $\pi/2$ pulse (100 μs in duration) to store the surface ^{77}Se magnetization along the main magnetic field (i.e. Z-magnetization) and allow for ^{77}Se-^{77}Se spin diffusion to core sites.[76] The ^{77}Se spin diffusion period was varied from 0.1 s to 600 s. ^{77}Se refocused-INADEQUATE-CPMG experiments were acquired with a 6 ms scalar coupling evolution time (τ_J), corresponding to 24 ms of total *J*-evolution. Experimental recycle delays, number of scans, indirect dimension time domain (TD) points, CPMG parameters and experimental time of experiments mentioned above are given in Table S2.

All ^{77}Se-^{113}Cd heteronuclear correlation NMR experiments were enabled by applying a REDOR box RF frequency splitter to the X-channel of the NMR probe to split the resonance frequency to both ^{77}Se and ^{113}Cd (Figure S9). The Y- and X-preamplifiers/amplifiers were assigned to ^{77}Se and ^{113}Cd, respectively, and connected to the REDOR box through a T-joint. Adjustable RF filters (Wavetek) were placed in between the preamplifiers and the REDOR box to isolate both channels (Figure S9); ^{77}Se filter (Y-amplifier): 0.376 dB at 76.4 MHz and-72.04 dB at 88.7 MHz, ^{113}Cd filter (X-amplifier): -55.17 dB at 76.3 MHz and 0.270 dB at 88.5 MHz. The efficiencies of the ^{77}Se and ^{113}Cd channels with the REDOR box were determined by comparing the RF field on both channels at the same power with the REDOR box to those in ^{1}H-X double resonance mode. There was a minimal loss in efficiency for ^{77}Se (60 W of input power gave a 61 kHz RF field without the REDOR box and 56 kHz with the REDOR box) while for the ^{113}Cd channel the efficiency with the REDOR box dropped

significantly (150 W of input power gave an RF field of 103 kHz without the REDOR box and 31 kHz with the REDOR box).

^{77}Se{^{113}Cd} *J*-HMQC experiments were recorded with ^{1}H→^{77}Se CP at the beginning of the experiment, CPMG for detection and 10 kHz MAS. ^{77}Se{^{113}Cd} *J*-HMQC experiments were performed by incrementing the *J*-evolution periods (τ) by integer multiples of rotor cycles. 1D ^{77}Se{^{113}Cd} *J*-HMQC optimizations of the ^{77}Se-^{113}Cd *J*-evolution periods were recorded with hard ^{77}Se refocusing pulses (7.5 or 8.25 μs) and either hard (7.25 or 8.25 μs) or selective (1 rotor cycle: 100 μs, 2.5 kHz RF field) π/2 excitation and reconversion pulses. The ^{77}Se transmitter was placed in between the surface and core ^{77}Se NMR signals (– 575 ppm). Experiments were then performed with the ^{113}Cd transmitter placed on resonance with the core (–55 ppm), the surface (–320 ppm), or in between the core and surface ^{113}Cd NMR signals (–200 ppm). The selectivity of the 1 rotor cycle (100 μs) ^{113}Cd π/2 pulse was checked through a ^{1}H→^{113}Cd CP-flip back-store-read sequence with a hard π/2 flip-back pulse and selective π/2 read pulse (Figure S10). ^{77}Se{^{113}Cd} heteronuclear *J*-resolved experiments were recorded with ^{1}H→^{77}Se CP at the beginning of the experiment, CPMG for detection, hard ^{77}Se π refocusing pulses (7.5 or 8.25 μs), and hard (14.5 or 16.5 μs) ^{113}Cd π refocusing pulses.

^{77}Se{^{113}Cd} *J*-resolved experiments were performed in a constant-time fashion to eliminate effects of homogeneous ^{77}Se transverse relaxation. The ^{77}Se spin echo period was fixed to an integer multiple of rotor cycles and the position of the ^{113}Cd refocusing pulse during the first echo period was incremented until it centers with the ^{77}Se

refocusing pulse (Figure S6). ^{113}Cd{^{77}Se} *J*-resolved experiments were recorded with ^{1}H→^{113}Cd CP at the beginning of the experiment and CPMG detection. The ^{113}Cd{^{77}Se} *J*-resolved experiments were performed with hard ^{77}Se and ^{113}Cd refocusing pulses (indicated above), with the ^{77}Se transmitter placed in between the core and surface NMR signals and the ^{113}Cd transmitter on resonance with the surface NMR signal.

Analytical fitting of experimental *J*-resolved and *J*-HMQC curves is described in the Supporting Information.

Supporting Information

Additional experimental details, powder XRD patterns, TEM micrographs, FTIR spectra, and additional solid-state NMR spectra.

Author Contributions

[†]Y.C. and R.W.D. contributed equally.

Acknowledgements

DNP-enhanced solid-state NMR experiments and data analysis (Y.C., R.W.D, M.P.H., A.J.R.) were supported by the U.S. Department of Energy (DOE), Office of Science, Basic Energy Sciences, Materials Science and Engineering Division. A.H.F. is grateful to the U.S. Department of Energy Office of Science Undergraduate Laboratory Internship (SULI) program for the assistantship and opportunity to participate in the SULI program. The Ames Laboratory is operated for the U.S. DOE by Iowa State

University under Contract DE-AC02-07CH11358. Nanocrystal synthesis, surface chemistry and IR spectroscopy (Y.C., L.W., R.B-F., A.M.M-G., M.A.S.A., J.V.) was supported by the U.S. National Science Foundation Division of Chemistry, Macromolecular, Supramolecular and Nanochemistry program (1905066). Electron microscopy of CdSe NCs was performed at the Sensitive Instrument Facility of the Ames Laboratory, which is operated for the U.S. Department of Energy by Iowa State University under Contract No. DE-AC02-07CH11358. A.J.R. acknowledges additional support from the Alfred P. Sloan Foundation through a Sloan research fellowship.

References

(1) Colvin, V. L.; Schlamp, M. C.; Alivisatos, A. P., Light-emitting diodes made from cadmium selenide nanocrystals and a semiconducting polymer. *Nature* **1994,** *370* (6488), 354-357.
(2) Huynh, W. U.; Dittmer, J. J.; Alivisatos, A. P., Hybrid Nanorod-Polymer Solar Cells. *Science* **2002,** *295* (5564), 2425.
(3) Gur, I.; Fromer, N. A.; Geier, M. L.; Alivisatos, A. P., Air-Stable All-Inorganic Nanocrystal Solar Cells Processed from Solution. *Science* **2005,** *310* (5747), 462.
(4) Talapin, D. V.; Lee, J.-S.; Kovalenko, M. V.; Shevchenko, E. V., Prospects of Colloidal Nanocrystals for Electronic and Optoelectronic Applications. *Chem. Rev.* **2010,** *110* (1), 389-458.
(5) Shirasaki, Y.; Supran, G. J.; Bawendi, M. G.; Bulović, V., Emergence of colloidal quantum-dot light-emitting technologies. *Nat. Photonics* **2013,** *7* (1), 13-23.
(6) Chuang, C.-H. M.; Brown, P. R.; Bulović, V.; Bawendi, M. G., Improved performance and stability in quantum dot solar cells through band alignment engineering. *Nat. Mater.* **2014,** *13* (8), 796-801.
(7) Kagan, C. R.; Lifshitz, E.; Sargent, E. H.; Talapin, D. V., Building devices from colloidal quantum dots. *Science* **2016,** *353* (6302), aac5523.
(8) Bruchez, M.; Moronne, M.; Gin, P.; Weiss, S.; Alivisatos, A. P., Semiconductor Nanocrystals as Fluorescent Biological Labels. *Science* **1998,** *281* (5385), 2013.
(9) Liu, W.; Howarth, M.; Greytak, A. B.; Zheng, Y.; Nocera, D. G.; Ting, A. Y.; Bawendi, M. G., Compact Biocompatible Quantum Dots Functionalized for Cellular Imaging. *J. Am. Chem. Soc.* **2008,** *130* (4), 1274-1284.
(10) Kim, S.; Lim, Y. T.; Soltesz, E. G.; De Grand, A. M.; Lee, J.; Nakayama, A.; Parker, J. A.; Mihaljevic, T.; Laurence, R. G.; Dor, D. M.; Cohn, L. H.; Bawendi, M. G.; Frangioni, J. V., Near-infrared fluorescent type II quantum dots for sentinel lymph node mapping. *Nat.*

Biotechnol. **2004,** *22* (1), 93-97.
(11) Weiss, E. A., Designing the Surfaces of Semiconductor Quantum Dots for Colloidal Photocatalysis. *ACS Energy Letters* **2017,** *2* (5), 1005-1013.
(12) Yin, Y.; Alivisatos, A. P., Colloidal nanocrystal synthesis and the organic–inorganic interface. *Nature* **2005,** *437* (7059), 664-670.
(13) Owen, J., The coordination chemistry of nanocrystal surfaces. *Science* **2015,** *347* (6222), 615-616.
(14) Boles, M. A.; Ling, D.; Hyeon, T.; Talapin, D. V., The surface science of nanocrystals. *Nat. Mater.* **2016,** *15* (2), 141-153.
(15) Smith, A. M.; Nie, S., Semiconductor Nanocrystals: Structure, Properties, and Band Gap Engineering. *Acc. Chem. Res.* **2010,** *43* (2), 190-200.
(16) Rogach, A. L.; Eychmüller, A.; Hickey, S. G.; Kershaw, S. V., Infrared-Emitting Colloidal Nanocrystals: Synthesis, Assembly, Spectroscopy, and Applications. *Small* **2007,** *3* (4), 536-557.
(17) Burda, C.; Chen, X.; Narayanan, R.; El-Sayed, M. A., Chemistry and Properties of Nanocrystals of Different Shapes. *Chemical Reviews* **2005,** *105* (4), 1025-1102.
(18) Moreels, I.; Lambert, K.; De Muynck, D.; Vanhaecke, F.; Poelman, D.; Martins, J. C.; Allan, G.; Hens, Z., Composition and Size-Dependent Extinction Coefficient of Colloidal PbSe Quantum Dots. *Chemistry of Materials* **2007,** *19* (25), 6101-6106.
(19) Vela, J., Molecular Chemistry to the Fore: New Insights into the Fascinating World of Photoactive Colloidal Semiconductor Nanocrystals. *The Journal of Physical Chemistry Letters* **2013,** *4* (4), 653-668.
(20) Bullen, C.; Mulvaney, P., The Effects of Chemisorption on the Luminescence of CdSe Quantum Dots. *Langmuir* **2006,** *22* (7), 3007-3013.
(21) Frederick, M. T.; Weiss, E. A., Relaxation of Exciton Confinement in CdSe Quantum Dots by Modification with a Conjugated Dithiocarbamate Ligand. *ACS Nano* **2010,** *4* (6), 3195-3200.
(22) Nagpal, P.; Klimov, V. I., Role of mid-gap states in charge transport and photoconductivity in semiconductor nanocrystal films. *Nature Communications* **2011,** *2* (1), 486.
(23) Hartley, C. L.; Kessler, M. L.; Dempsey, J. L., Molecular-Level Insight into Semiconductor Nanocrystal Surfaces. *J. Am. Chem. Soc.* **2021**.
(24) Moreels, I.; Fritzinger, B.; Martins, J. C.; Hens, Z., Surface Chemistry of Colloidal PbSe Nanocrystals. *J. Am. Chem. Soc.* **2008,** *130* (45), 15081-15086.
(25) Cros-Gagneux, A.; Delpech, F.; Nayral, C.; Cornejo, A.; Coppel, Y.; Chaudret, B., Surface Chemistry of InP Quantum Dots: A Comprehensive Study. *J. Am. Chem. Soc.* **2010,** *132* (51), 18147-18157.
(26) Hens, Z.; Martins, J. C., A Solution NMR Toolbox for Characterizing the Surface Chemistry of Colloidal Nanocrystals. *Chem. Mater.* **2013,** *25* (8), 1211-1221.
(27) De Roo, J.; Ibáñez, M.; Geiregat, P.; Nedelcu, G.; Walravens, W.; Maes, J.; Martins, J. C.; Van Driessche, I.; Kovalenko, M. V.; Hens, Z., Highly Dynamic Ligand Binding and Light Absorption Coefficient of Cesium Lead Bromide Perovskite Nanocrystals. *ACS Nano* **2016,** *10* (2), 2071-2081.
(28) Knauf, R. R.; Lennox, J. C.; Dempsey, J. L., Quantifying Ligand Exchange Reactions at CdSe Nanocrystal Surfaces. *Chem. Mater.* **2016,** *28* (13), 4762-4770.
(29) Drijvers, E.; De Roo, J.; Martins, J. C.; Infante, I.; Hens, Z., Ligand Displacement Exposes

Binding Site Heterogeneity on CdSe Nanocrystal Surfaces. *Chem. Mater.* **2018,** *30* (3), 1178-1186.
(30) De Roo, J.; Yazdani, N.; Drijvers, E.; Lauria, A.; Maes, J.; Owen, J. S.; Van Driessche, I.; Niederberger, M.; Wood, V.; Martins, J. C.; Infante, I.; Hens, Z., Probing Solvent–Ligand Interactions in Colloidal Nanocrystals by the NMR Line Broadening. *Chem. Mater.* **2018,** *30* (15), 5485-5492.
(31) Smock, S. R.; Williams, T. J.; Brutchey, R. L., Quantifying the Thermodynamics of Ligand Binding to CsPbBr3 Quantum Dots. *Angew. Chem. Int. Ed.* **2018,** *57* (36), 11711-11715.
(32) Zhang, J.; Zhang, H.; Cao, W.; Pang, Z.; Li, J.; Shu, Y.; Zhu, C.; Kong, X.; Wang, L.; Peng, X., Identification of Facet-Dependent Coordination Structures of Carboxylate Ligands on CdSe Nanocrystals. *J. Am. Chem. Soc.* **2019,** *141* (39), 15675-15683.
(33) Ip, A. H.; Thon, S. M.; Hoogland, S.; Voznyy, O.; Zhitomirsky, D.; Debnath, R.; Levina, L.; Rollny, L. R.; Carey, G. H.; Fischer, A.; Kemp, K. W.; Kramer, I. J.; Ning, Z.; Labelle, A. J.; Chou, K. W.; Amassian, A.; Sargent, E. H., Hybrid passivated colloidal quantum dot solids. *Nature Nanotechnology* **2012,** *7* (9), 577-582.
(34) Zherebetskyy, D.; Scheele, M.; Zhang, Y.; Bronstein, N.; Thompson, C.; Britt, D.; Salmeron, M.; Alivisatos, P.; Wang, L.-W., Hydroxylation of the surface of PbS nanocrystals passivated with oleic acid. *Science* **2014,** *344* (6190), 1380.
(35) Ning, Z.; Gong, X.; Comin, R.; Walters, G.; Fan, F.; Voznyy, O.; Yassitepe, E.; Buin, A.; Hoogland, S.; Sargent, E. H., Quantum-dot-in-perovskite solids. *Nature* **2015,** *523* (7560), 324-328.
(36) Houtepen, A. J.; Hens, Z.; Owen, J. S.; Infante, I., On the Origin of Surface Traps in Colloidal II–VI Semiconductor Nanocrystals. *Chem. Mater.* **2017,** *29* (2), 752-761.
(37) Giansante, C.; Infante, I., Surface Traps in Colloidal Quantum Dots: A Combined Experimental and Theoretical Perspective. *The Journal of Physical Chemistry Letters* **2017,** *8* (20), 5209-5215.
(38) du Fossé, I.; ten Brinck, S.; Infante, I.; Houtepen, A. J., Role of Surface Reduction in the Formation of Traps in n-Doped II–VI Semiconductor Nanocrystals: How to Charge without Reducing the Surface. *Chemistry of Materials* **2019,** *31* (12), 4575-4583.
(39) Goldzak, T.; McIsaac, A. R.; Van Voorhis, T., Colloidal CdSe nanocrystals are inherently defective. *Nat. Commun.* **2021,** *12* (1), 890.
(40) Thayer, A. M.; Steigerwald, M. L.; Duncan, T. M.; Douglass, D. C., NMR Study of Semiconductor Molecular Clusters. *Phys. Rev. Lett.* **1988,** *60* (25), 2673-2676.
(41) Tomaselli, M.; Yarger, J. L.; Bruchez, M.; Havlin, R. H.; deGraw, D.; Pines, A.; Alivisatos, A. P., NMR study of InP quantum dots: Surface structure and size effects. *The Journal of Chemical Physics* **1999,** *110* (18), 8861-8864.
(42) Cadars, S.; Smith, B. J.; Epping, J. D.; Acharya, S.; Belman, N.; Golan, Y.; Chmelka, B. F., Atomic Positional Versus Electronic Order in Semiconducting ZnSe Nanoparticles. *Phys. Rev. Lett.* **2009,** *103* (13), 136802.
(43) Loyingood, D. D.; Achey, R.; Paravastu, A. K.; Strouse, G. F., Size- and Site-Dependent Reconstruction in CdSe QDs Evidenced by ^{77}Se{^{1}H} CP-MAS NMR Spectroscopy. *J. Am. Chem. Soc.* **2010,** *132* (10), 3344-3354.
(44) Yesinowski, J. P., Solid-State NMR of Inorganic Semiconductors. *Solid State NMR* **2012,** *306*, 229-312.

(45) Thiessen, A. N.; Ha, M.; Hooper, R. W.; Yu, H.; Oliynyk, A. O.; Veinot, J. G. C.; Michaelis, V. K., Silicon Nanoparticles: Are They Crystalline from the Core to the Surface? *Chemistry of Materials* **2019,** *31* (3), 678-688.
(46) Chen, Y.; Smock, S. R.; Flintgruber, A. H.; Perras, F. A.; Brutchey, R. L.; Rossini, A. J., Surface Termination of CsPbBr3 Perovskite Quantum Dots Determined by Solid-State NMR Spectroscopy. *J. Am. Chem. Soc.* **2020,** *142* (13), 6117-6127.
(47) Mikulec, F. V.; Kuno, M.; Bennati, M.; Hall, D. A.; Griffin, R. G.; Bawendi, M. G., Organometallic Synthesis and Spectroscopic Characterization of Manganese-Doped CdSe Nanocrystals. *J. Am. Chem. Soc.* **2000,** *122* (11), 2532-2540.
(48) Ladizhansky, V.; Hodes, G.; Vega, S., Surface Properties of Precipitated CdS Nanoparticles Studied by NMR. *J. Phys. Chem. B* **1998,** *102* (43), 8505-8509.
(49) Berrettini, M. G.; Braun, G.; Hu, J. G.; Strouse, G. F., NMR Analysis of Surfaces and Interfaces in 2-nm CdSe. *Journal of the American Chemical Society* **2004,** *126* (22), 7063-7070.
(50) Ratcliffe, C. I.; Yu, K.; Ripmeester, J. A.; Badruz Zaman, M.; Badarau, C.; Singh, S., Solid state NMR studies of photoluminescent cadmium chalcogenide nanoparticles. *Phys. Chem. Chem. Phys.* **2006,** *8* (30), 3510-3519.
(51) Li, M.; Ouyang, J.; Ratcliffe, C. I.; Pietri, L.; Wu, X.; Leek, D. M.; Moudrakovski, I.; Lin, Q.; Yang, B.; Yu, K., CdS Magic-Sized Nanocrystals Exhibiting Bright Band Gap Photoemission via Thermodynamically Driven Formation. *ACS Nano* **2009,** *3* (12), 3832-3838.
(52) Wang, R.; Ratcliffe, C. I.; Wu, X.; Voznyy, O.; Tao, Y.; Yu, K., Magic-Sized Cd3P2 II−V Nanoparticles Exhibiting Bandgap Photoemission. *J. Phys. Chem. C* **2009,** *113* (42), 17979-17982.
(53) Lelli, M.; Gajan, D.; Lesage, A.; Caporini, M. A.; Vitzthum, V.; Miéville, P.; Héroguel, F.; Rascón, F.; Roussey, A.; Thieuleux, C.; Boualleg, M.; Veyre, L.; Bodenhausen, G.; Coperet, C.; Emsley, L., Fast Characterization of Functionalized Silica Materials by Silicon-29 Surface-Enhanced NMR Spectroscopy Using Dynamic Nuclear Polarization. *Journal of the American Chemical Society* **2011,** *133* (7), 2104-2107.
(54) Virieux, H.; Le Troedec, M.; Cros-Gagneux, A.; Ojo, W.-S.; Delpech, F.; Nayral, C.; Martinez, H.; Chaudret, B., InP/ZnS Nanocrystals: Coupling NMR and XPS for Fine Surface and Interface Description. *J. Am. Chem. Soc.* **2012,** *134* (48), 19701-19708.
(55) Lee, D.; Duong, N. T.; Lafon, O.; De Paëpe, G., Primostrato Solid-State NMR Enhanced by Dynamic Nuclear Polarization: Pentacoordinated Al3+ Ions Are Only Located at the Surface of Hydrated γ-Alumina. *The Journal of Physical Chemistry C* **2014,** *118* (43), 25065-25076.
(56) Piveteau, L.; Ong, T.-C.; Rossini, A. J.; Emsley, L.; Coperet, C.; Kovalenko, M. V., Structure of colloidal quantum dots from dynamic nuclear polarization surface enhanced NMR spectroscopy. *J. Am. Chem. Soc.* **2015,** *137* (43), 13964-13971.
(57) Piveteau, L.; Ong, T.-C.; Walder, B. J.; Dirin, D. N.; Moscheni, D.; Schneider, B.; Bär, J.; Protesescu, L.; Masciocchi, N.; Guagliardi, A.; Emsley, L.; Copéret, C.; Kovalenko, M. V., Resolving the Core and the Surface of CdSe Quantum Dots and Nanoplatelets Using Dynamic Nuclear Polarization Enhanced PASS–PIETA NMR Spectroscopy. *ACS Cent. Sci.* **2018,** *4* (9), 1113-1125.
(58) Tessier, M. D.; Baquero, E. A.; Dupont, D.; Grigel, V.; Bladt, E.; Bals, S.; Coppel, Y.; Hens, Z.; Nayral, C.; Delpech, F., Interfacial Oxidation and Photoluminescence of InP-Based Core/Shell Quantum Dots. *Chem. Mater.* **2018,** *30* (19), 6877-6883.

(59) Piveteau, L.; Dirin, D. N.; Gordon, C. P.; Walder, B. J.; Ong, T.-C.; Emsley, L.; Copéret, C.; Kovalenko, M. V., Colloidal-ALD-Grown Core/Shell CdSe/CdS Nanoplatelets as Seen by DNP Enhanced PASS–PIETA NMR Spectroscopy. *Nano Lett.* **2020,** *20* (5), 3003-3018.
(60) Ni, Q. Z.; Daviso, E.; Can, T. V.; Markhasin, E.; Jawla, S. K.; Swager, T. M.; Temkin, R. J.; Herzfeld, J.; Griffin, R. G., High Frequency Dynamic Nuclear Polarization. *Acc. Chem. Res.* **2013,** *46* (9), 1933-1941.
(61) Rossini, A. J.; Zagdoun, A.; Lelli, M.; Lesage, A.; Copéret, C.; Emsley, L., Dynamic Nuclear Polarization Surface Enhanced NMR Spectroscopy. *Accounts of Chemical Research* **2013,** *46* (9), 1942-1951.
(62) Hanrahan, M. P.; Chen, Y.; Blome-Fernández, R.; Stein, J. L.; Pach, G. F.; Adamson, M. A. S.; Neale, N. R.; Cossairt, B. M.; Vela, J.; Rossini, A. J., Probing the Surface Structure of Semiconductor Nanoparticles by DNP SENS with Dielectric Support Materials. *J. Am. Chem. Soc.* **2019,** *141* (39), 15532-15546.
(63) Viger-Gravel, J.; Berruyer, P.; Gajan, D.; Basset, J.-M.; Lesage, A.; Tordo, P.; Ouari, O.; Emsley, L., Frozen Acrylamide Gels as Dynamic Nuclear Polarization Matrices. *Angew. Chem. Int. Ed.* **2017,** *56* (30), 8726-8730.
(64) Chen, O.; Chen, X.; Yang, Y.; Lynch, J.; Wu, H.; Zhuang, J.; Cao, Y. C., Synthesis of Metal–Selenide Nanocrystals Using Selenium Dioxide as the Selenium Precursor. *Angewandte Chemie International Edition* **2008,** *47* (45), 8638-8641.
(65) Chen, O.; Yang, Y.; Wang, T.; Wu, H.; Niu, C.; Yang, J.; Cao, Y. C., Surface-Functionalization-Dependent Optical Properties of II–VI Semiconductor Nanocrystals. *J. Am. Chem. Soc.* **2011,** *133* (43), 17504-17512.
(66) Ithurria, S.; Dubertret, B., Quasi 2D Colloidal CdSe Platelets with Thicknesses Controlled at the Atomic Level. *J. Am. Chem. Soc.* **2008,** *130* (49), 16504-16505.
(67) Chen, Y.; Chen, D.; Li, Z.; Peng, X., Symmetry-Breaking for Formation of Rectangular CdSe Two-Dimensional Nanocrystals in Zinc-Blende Structure. *J. Am. Chem. Soc.* **2017,** *139* (29), 10009-10019.
(68) Singh, S.; Tomar, R.; ten Brinck, S.; De Roo, J.; Geiregat, P.; Martins, J. C.; Infante, I.; Hens, Z., Colloidal CdSe Nanoplatelets, A Model for Surface Chemistry/Optoelectronic Property Relations in Semiconductor Nanocrystals. *J. Am. Chem. Soc.* **2018,** *140* (41), 13292-13300.
(69) Taylor, J.; Kippeny, T.; Rosenthal, S. J., Surface Stoichiometry of CdSe Nanocrystals Determined by Rutherford Backscattering Spectroscopy. *Journal of Cluster Science* **2001,** *12* (4), 571-582.
(70) Fritzinger, B.; Capek, R. K.; Lambert, K.; Martins, J. C.; Hens, Z., Utilizing Self-Exchange To Address the Binding of Carboxylic Acid Ligands to CdSe Quantum Dots. *J. Am. Chem. Soc.* **2010,** *132* (29), 10195-10201.
(71) Karel Čapek, R.; Moreels, I.; Lambert, K.; De Muynck, D.; Zhao, Q.; Van Tomme, A.; Vanhaecke, F.; Hens, Z., Optical Properties of Zincblende Cadmium Selenide Quantum Dots. *The Journal of Physical Chemistry C* **2010,** *114* (14), 6371-6376.
(72) De Nolf, K.; Cosseddu, S. M.; Jasieniak, J. J.; Drijvers, E.; Martins, J. C.; Infante, I.; Hens, Z., Binding and Packing in Two-Component Colloidal Quantum Dot Ligand Shells: Linear versus Branched Carboxylates. *J. Am. Chem. Soc.* **2017,** *139* (9), 3456-3464.
(73) Yu, W. W.; Qu, L.; Guo, W.; Peng, X., Experimental Determination of the Extinction

Coefficient of CdTe, CdSe, and CdS Nanocrystals. *Chem. Mater.* **2003,** *15* (14), 2854-2860.
(74) Ithurria, S.; Bousquet, G.; Dubertret, B., Continuous Transition from 3D to 1D Confinement Observed during the Formation of CdSe Nanoplatelets. *J. Am. Chem. Soc.* **2011,** *133* (9), 3070-3077.
(75) Björgvinsdóttir, S.; Walder, B. J.; Matthey, N.; Emsley, L., Maximizing nuclear hyperpolarization in pulse cooling under MAS. *J. Magn. Reson.* **2019,** *300*, 142-148.
(76) Björgvinsdóttir, S.; Walder, B. J.; Pinon, A. C.; Emsley, L., Bulk Nuclear Hyperpolarization of Inorganic Solids by Relay from the Surface. *J. Am. Chem. Soc.* **2018,** *140* (25), 7946-7951.
(77) Hu, J. Z.; Wang, W.; Liu, F.; Solum, M. S.; Alderman, D. W.; Pugmire, R. J.; Grant, D. M., Magic-Angle-Turning Experiments for Measuring Chemical-Shift-Tensor Principal Values in Powdered Solids. *J. Magn. Reson. A* **1995,** *113* (2), 210-222.
(78) Nolle, A., Isotropie and Anisotropie Nuclear Magnetic Shielding of 113Cd in Cadmiumhalides, Cadmiumchalcogenides and in Cadmiumcarbonate. *Z. Naturforsch.* **1978,** *33* (6), 666-671.
(79) Lesage, A.; Auger, C.; Caldarelli, S.; Emsley, L., Determination of Through-Bond Carbon−Carbon Connectivities in Solid-State NMR Using the INADEQUATE Experiment. *J. Am. Chem. Soc.* **1997,** *119* (33), 7867-7868.
(80) Rossini, A. J.; Hanrahan, M. P.; Thuo, M., Rapid acquisition of wideline MAS solid-state NMR spectra with fast MAS, proton detection, and dipolar HMQC pulse sequences. *Phys. Chem. Chem. Phys.* **2016,** *18* (36), 25284-25295.
(81) Massiot, D.; Fayon, F.; Deschamps, M.; Cadars, S.; Florian, P.; Montouillout, V.; Pellerin, N.; Hiet, J.; Rakhmatullin, A.; Bessada, C., Detection and use of small J couplings in solid state NMR experiments. *C. R. Chim.* **2010,** *13* (1), 117-129.
(82) Massiot, D.; Fayon, F.; Alonso, B.; Trebosc, J.; Amoureux, J.-P., Chemical bonding differences evidenced from J-coupling in solid state NMR experiments involving quadrupolar nuclei. *J. Magn. Reson.* **2003,** *164* (1), 160-164.
(83) Lesage, A.; Sakellariou, D.; Steuernagel, S.; Emsley, L., Carbon−Proton Chemical Shift Correlation in Solid-State NMR by Through-Bond Multiple-Quantum Spectroscopy. *J. Am. Chem. Soc.* **1998,** *120* (50), 13194-13201.
(84) Pourpoint, F.; Trébosc, J.; Gauvin, R. M.; Wang, Q.; Lafon, O.; Deng, F.; Amoureux, J.-P., Measurement of Aluminum–Carbon Distances Using S-RESPDOR NMR Experiments. *ChemPhysChem* **2012,** *13* (16), 3605-3615.
(85) Pourpoint, F.; Morin, Y.; Gauvin, R. M.; Trébosc, J.; Capet, F.; Lafon, O.; Amoureux, J.-P., Advances in Structural Studies on Alkylaluminum Species in the Solid State via Challenging 27Al–13C NMR Spectroscopy and X-ray Diffraction. *The Journal of Physical Chemistry C* **2013,** *117* (35), 18091-18099.
(86) Perras, F. A.; Padmos, J. D.; Johnson, R. L.; Wang, L. L.; Schwartz, T. J.; Kobayashi, T.; Horton, J. H.; Dumesic, J. A.; Shanks, B. H.; Johnson, D. D.; Pruski, M., Characterizing Substrate-Surface Interactions on Alumina-Supported Metal Catalysts by Dynamic Nuclear Polarization-Enhanced Double-Resonance NMR Spectroscopy. *J. Am. Chem. Soc.* **2017,** *139* (7), 2702-2709.
(87) Demko, B. A.; Wasylishen, R. E., A solid-state NMR investigation of single-source precursors for group 12 metal selenides; M[N(iPr2PSe)2]2 (M = Zn, Cd, Hg). *Dalton Trans.*

2008, (4), 481-490.
(88) Barrie, P. J.; Clark, R. J. H.; Withnall, R.; Chung, D.-Y.; Kim, K.-W.; Kanatzidis, M. G., 77Se Solid-State NMR Studies of [M(Se4)2]2- Anions (M = Zn, Cd, Hg). *Inorganic Chemistry* **1994,** *33* (6), 1212-1216.
(89) Carson, G. K.; Dean, P. A. W., A selenium-77 and cadmium-113 NMR spectroscopic study of phenylselenolate complexes of cadmium. *Inorganica Chimica Acta* **1982,** *66*, 37-39.
(90) Kubo, A.; McDowell, C. A., One- and two-dimensional 31P cross-polarization magic-angle-spinning nuclear magnetic resonance studies on two-spin systems with homonuclear dipolar coupling and J coupling. *J. Chem. Phys.* **1990,** *92* (12), 7156-7170.
(91) Wu, G.; Wasylishen, R. E., Homonuclear phosphorus-31 J-resolved 2D spectra of rhodium(I) phosphine complexes in the solid state. *Inorg. Chem.* **1992,** *31* (1), 145-148.
(92) Bak, M.; Rasmussen, J. T.; Nielsen, N. C., SIMPSON: A General Simulation Program for Solid-State NMR Spectroscopy. *J. Magn. Reson.* **2000,** *147* (2), 296-330.
(93) Wang, Z.; Hanrahan, M. P.; Kobayashi, T.; Perras, F. A.; Chen, Y.; Engelke, F.; Reiter, C.; Purea, A.; Rossini, A. J.; Pruski, M., Combining fast magic angle spinning dynamic nuclear polarization with indirect detection to further enhance the sensitivity of solid-state NMR spectroscopy. *Solid State Nucl. Magn. Reson.* **2020,** *109*, 101685.
(94) Matsuki, Y.; Ueda, K.; Idehara, T.; Ikeda, R.; Ogawa, I.; Nakamura, S.; Toda, M.; Anai, T.; Fujiwara, T., Helium-cooling and -spinning dynamic nuclear polarization for sensitivity-enhanced solid-state NMR at 14T and 30K. *J. Magn. Reson.* **2012,** *225*, 1-9.
(95) Thurber, K.; Tycko, R., Low-temperature dynamic nuclear polarization with helium-cooled samples and nitrogen-driven magic-angle spinning. *J. Magn. Reson.* **2016,** *264*, 99-106.
(96) Zhu, C.; Chen, D.; Cao, W.; Lai, R.; Pu, C.; Li, J.; Kong, X.; Peng, X., Facet-Dependent On-Surface Reactions in the Growth of CdSe Nanoplatelets. *Angew. Chem. Int. Ed.* **2019,** *58* (49), 17764-17770.
(97) Chen, O.; Chen, X.; Yang, Y.; Lynch, J.; Wu, H.; Zhuang, J.; Cao, Y. C., Synthesis of Metal–Selenide Nanocrystals Using Selenium Dioxide as the Selenium Precursor. *Angew. Chem. Int. Ed.* **2008,** *47* (45), 8638-8641.
(98) Metz, G.; Wu, X. L.; Smith, S. O., Ramped-Amplitude Cross Polarization in Magic-Angle-Spinning NMR. *J. Magn. Reson. A* **1994,** *110* (2), 219-227.
(99) Fung, B. M.; Khitrin, A. K.; Ermolaev, K., An Improved Broadband Decoupling Sequence for Liquid Crystals and Solids. *J. Magn. Reson.* **2000,** *142* (1), 97-101.
(100) Harris, R. K.; Becker, E. D.; Cabral de Menezes, S. M.; Goodfellow, R.; Granger, P., NMR nomenclature. Nuclear spin properties and conventions for chemical shifts(IUPAC Recommendations 2001). *Pure Appl. Chem.* **2001,** *73* (11), 1795-1818.
(101) Trebosc, J.; Wiench, J. W.; Huh, S.; Lin, V. S. Y.; Pruski, M., Studies of Organically Functionalized Mesoporous Silicas Using Heteronuclear Solid-State Correlation NMR Spectroscopy under Fast Magic Angle Spinning. *J. Am. Chem. Soc.* **2005,** *127* (20), 7587-7593.
(102) Duma, L.; Lai, W. C.; Carravetta, M.; Emsley, L.; Brown, S. P.; Levitt, M. H., Principles of Spin-Echo Modulation by J-Couplings in Magic-Angle-Spinning Solid-State NMR. *ChemPhysChem* **2004,** *5* (6), 815-833.

Supporting Information for:

Revealing the Surface Structure of CdSe Nanocrystals by Dynamic Nuclear Polarization-Enhanced ^{77}Se and ^{113}Cd Solid-State NMR Spectroscopy.

Yunhua Chen,[1,2,†] Rick W. Dorn,[1,2,†] Michael P. Hanrahan,[1,2] Lin Wei,[2] Rafael Blome-Fernández,[2] Alan M. Medina-Gonzalez,[2] Marquix A. S. Adamson,[2] Anne H. Flintgruber,[1] Javier Vela[1,2]* and Aaron J. Rossini[1,2]*

[1]US Department of Energy, Ames Laboratory, Ames, IA, USA 50011.

[2]Department of Chemistry, Iowa State University, Ames, IA, USA 50011.

Table of Contents

Additional Experimental Details

Materials Characterization

Powder X-ray diffraction (XRD) was recorded using a Rigaku Ultima IV diffractometer with a Cu Kα radiation (40 kV, 44 mA). Scherrer analysis was performed with Jade using a κ value of 0.9**.**

Transmission electron microscopy (TEM) imaging was performed on an FEI Tecnai G2-F2 scanning transmission electron microscope.

Dynamic light scattering (DLS) was measured with a Malvern Zetasizer Nano ZS equipped with a 532 nm laser. Square plastic cells with a 12 mm (outer diameter) were used for all measurements.

Optical absorption characterization. Infrared (IR) spectroscopy measurements were performed on a Bruker Tensor 37 Fourier transform IR spectrophotometer (64 scans, transmittance mode). *UV-Vis absorbance* spectra were collected with a photodiode-array Agilent 8453 UV-Vis spectrometer. *Steady-state photoluminescence (PL)* was measured with a Horiba-Jobin Yvon Nanolog scanning spectrofluorometer equipped with a photomultiplier detector. Relative PL quantum yields (QYs) were measured following literature procedures, using Rhodamine 6G or Coumarin 540A in ethanol as standard.[1] Absorption and PL emission spectra were measured as replicated three or more, and the average QYs were recorded.

Analytical Fitting of Experimental *J*-Resolved and *J*-HMQC Curves.

General fitting of $^{77}Se\{^{113}Cd\}$ J-HMQC curves. In a *J*-HMQC experiment, the

NMR signal is built-up/modulated by $\sin(\pi J\tau)^2$, where J is scalar coupling and τ is the J-evolution period (Figure S6). The ^{77}Se{^{113}Cd} J-HMQC curves with selective π/2 pulse core ^{113}Cd NMR signals were fit using the equation below:

$$I_{HMQC} = \exp\left(-2\tau/T_2'\right) \sum_{J_n=1\,Hz}^{J_n=500\,Hz} \frac{c}{\sigma\sqrt{2\pi}} exp\left(-\frac{1}{2}\frac{(J_n - J)}{\sigma}\right) sin^2(\pi J_n \tau)$$

The ^{77}Se{^{113}Cd} J-HMQC curves with selective π/2 pulses on surface ^{113}Cd NMR signals were fit with two unique J-couplings and the following equation: $\text{Int.} = \text{A} \times \sin(\pi J\tau)^2 + B \times \sin(\pi J\tau)^2$, where A and B are equal scaling values. The J-coupling for each fit was taken from a Gaussian distribution to represent the J-coupling strengths' distribution due to the nanoparticles' structural disorder.

General fitting of J-resolved curves. In a heteronuclear J-resolved NMR experiment the NMR signal intensity of the detected spin will modulate by $\cos(2\pi J\tau)^n$, where J is the strength of the scalar (J-) coupling, τ is the J-evolution period (Figure 6) and n describes the number of J-coupled spins to the detect spin. However, when the natural isotopic abundance of the J-coupled spins to the detect spin is less than 100 %, the proper statistical distribution for the probability of having 0 to n J-coupled spins must be taken into account. The natural isotopic abundance of ^{77}Se and ^{113}Cd is 7.63 % and 12.22 %, respectively. Below the exact equations for analytical fits of all J-resolved curves are described.

^{77}Se{^{113}Cd} J-Resolved – Core Se species ($SeCd_{4,core}$). Each core Se atom is bonded to four core Cd atoms exhibiting the same relative J-coupling. However, due to structural disorder near the NC's surface, there is a distribution in the one bond Se-Cd J couplings ($^1J_{Se\text{-}Cd}$) described by a Gaussian distribution. Excluding the Gaussian

distribution in the $^{1}J_{\text{Se-Cd}}$, the following equation describes the general analytical equation used to fit the core Se ^{77}Se{^{113}Cd} *J*-resolved curves:

$$Eq.(1): Int. = 1 - 0.8778^4 + 4 \times \cos(\pi J \tau) \times 0.8778^3 \times 0.1222 + 6 \times \cos(\pi J \tau)^2 \times 0.8778^2 \times 0.1222^2 + 4 \times \cos(\pi J \tau)^3 \times 0.8778 \times 0.1222^3 + \cos(\pi J \tau)^4 \times 0.1222^4$$

^{77}Se{^{113}Cd} J-Resolved – Surface Se species ($SeCd_{2,core}Cd_{2,surface}$). As discussed in the main text, from the selective ^{77}Se{^{113}Cd} *J*-HMQC *J*-evolution curves, it is known that the surface Se atoms are bonded to 4 Cd atoms: 2 core like Cd atoms exhibiting the same $^{1}J_{\text{Se-Cd}}$ and 2 surface like Cd atoms with different $^{1}J_{\text{Se-Cd}}$. In addition, there is a distribution in each $^{1}J_{\text{Se-Cd}}$ due to structural disorder that can be described by a Gaussian distribution. Excluding the Gaussian distribution in the $^{1}J_{\text{Se-Cd}}$, the following equation describes the general analytical equation used to fit the surface Se ^{77}Se{^{113}Cd} *J*-Resolved curves (note that J_1 = surface $^{1}J_{\text{Se-Cd}}$ #1, J_2 = surface $^{1}J_{\text{Se-Cd}}$ #2 and J_3 = core $^{1}J_{\text{Se-Cd}}$):

$$Eq.(1): Int. = 1 - 0.8778^4 + f_{surface} \times \cos(\pi J_1 \tau) \times 0.8778^3 \times 0.1222 + f_{surface} \times \cos(\pi J_2 \tau) \times 0.8778^3 \times 0.1222 + 2 \times \cos(\pi J_3 \tau) \times 0.8778^3 \times 0.1222 + f_{surface}^2 \times \cos(\pi J_1 \tau) \times \cos(\pi J_2 \tau) \times 0.8778^2 \times 0.1222^2 + 2 \times f_{surface} \times \cos(\pi J_1 \tau) \times \cos(\pi J_3 \tau) \times 0.8778^2 \times 0.1222^2$$

$$+\ 2 \times f_{surface} \times \cos(\pi J_2 \tau) \times \cos(\pi J_3 \tau) \times 0.8778^2 \times 0.1222^2$$

$$+\ \cos(\pi J_3 \tau)^2 \times 0.8778^2 \times 0.1222^2$$

$$+\ 2 \times f_{surface}^2 \times \cos(\pi J_1 \tau) \times \cos(\pi J_2 \tau) \times \cos(\pi J_3 \tau) \times 0.8778 \times 0.1222^3$$

$$+ f_{surface} \times \cos(\pi J_1 \tau) \times \cos(\pi J_3 \tau)^2 \times 0.8778 \times 0.1222^3$$

$$+\ f_{surface} \times \cos(\pi J_2 \tau) \times \cos(\pi J_3 \tau)^2\ 0.8778 \times 0.1222^3$$

$$+\ f_{surface}^2 \times \cos(\pi J_1 \tau) \times \cos(\pi J_2 \tau) \times \cos(\pi J_3 \tau)^2 \times 0.1222^4$$

^{113}Cd{^{77}Se} J-Resolved – Surface Cd species ($CdSe_2O_2$). The surface Cd atoms are bonded to 2 O atoms from the surface ligands and 2 Se species one layer in (surface like Se). The 2 surface like Cd atoms exhibit different $^1J_{Se\text{-}Cd}$. In addition, there is a distribution in each $^1J_{Se\text{-}Cd}$ due to structural disorder that can be described by a Gaussian distribution. Excluding the Gaussian distribution in the $^1J_{Se\text{-}Cd}$, the following equation describes the general analytical equation used to fit the surface Cd ^{113}Cd{^{77}Se} *J*-resolved curves (note that J_1 = surface $^1J_{Se\text{-}Cd}$ #1 and J_2 = surface $^1J_{Se\text{-}Cd}$ #2):

$$Eq.(1): Int. = \ 1 - 0.9237^2$$

$$+\ f_{surface} \times \cos(\pi J_1 \tau) \times 0.9237 \times 0.0763$$

$$+\ f_{surface} \times \cos(\pi J_2 \tau) \times 0.9237 \times 0.0763$$

$$+ f_{surface}^2 \times \cos(\pi J_1 \tau) \times \cos(\pi J_2 \tau) \times 0.0763^2$$

Table S1. NMR experimental parameters (^{1}H spin-lock RF fields, X spin-lock RF fields, CP contact times, X or Y channel π/2 or π pulse RF fields, MAS Frequency and ^{113}Cd transmitter offset)

Experiment	^{1}H Spin-lock RF (kHz)	X Spin-lock RF (kHz)	CP Contact Time (μs)	X or Y channel π/2 or π pulse RF Field (kHz)	MAS Frequency (kHz)	^{113}Cd Transmitter Offset (ppm)
CdSe nanoplatelets						
^{13}C CP spin echo (microwave Off)	79	53	1000	^{13}C, 62.5	10	
^{13}C CP spin echo (microwave On)	79	53	1000	^{13}C, 62.5	10	
^{113}Cd CP-CPMG	100	75	500 2000 8000	^{113}Cd, 62.5	10	
^{113}Cd CP pulse cooling	-	-	-	-	-	
^{113}Cd-^{113}Cd CP-MAT	100	75	8000	^{113}Cd, 71.4	9.009	
^{113}Cd-^{113}Cd refocused-INADEQUATE-CPMG	100	75	8000	^{113}Cd, 100	10	
^{77}Se CP-CPMG	63	51	500 2000 9000	^{77}Se, 83.3	10	
^{77}Se CP spin diffusion	-	-	-	-	-	
^{77}Se-^{77}Se refocused-INADEQUATE-CPMG	68	51	9000	^{77}Se, 83.3	10	
^{77}Se{^{113}Cd} 2D *J*-HMQC	48	55	9000	^{77}Se, 60.6 ^{113}Cd, 34.5	10	– 200
^{77}Se{^{113}Cd} *J*-HMQC curve	48	55	9000	^{77}Se, 60.6 ^{113}Cd, 2.5	10	– 55
	48	55	9000	^{77}Se, 60.6 ^{113}Cd, 2.5	10	– 320
	48	55	9000	^{77}Se, 60.6 ^{113}Cd, 34.5	10	– 200
^{77}Se{^{113}Cd} *J*-resolved curve	50	55	9000	^{77}Se, 60.6 ^{113}Cd, 2.3	9.009	– 55
	50	55	9000	^{77}Se, 60.6	9.009	– 320

				^{113}Cd, 2.3		
	50	55	9000	^{77}Se, 60.6 ^{113}Cd, 34.5	10	– 55
	50	55	9000	^{77}Se, 60.6 ^{113}Cd, 34.5	10	– 200
	50	55	9000	^{77}Se, 60.6 ^{113}Cd, 34.5	10	– 320
^{113}Cd{^{77}Se} *J*-resolved curve	50	28	8000	^{113}Cd, 34.5 ^{77}Se, 60.6	10	– 320
CdSe nanospheroids						
^{13}C CP spin echo (microwave Off)	79	53	1000	^{13}C, 62.5	10	
^{13}C CP spin echo (microwave On)	79	53	1000	^{13}C, 62.5	10	
^{113}Cd CP-CPMG	82	89	250 2000 7000	^{113}Cd, 100	10	
^{113}Cd CP pulse cooling	82	89	5000	^{113}Cd, 100	10	
^{113}Cd-^{113}Cd CP-MAT	82	89	7000	^{113}Cd, 100	10	
^{113}Cd-^{113}Cd refocused-INADEQUATE-CPMG	82	89	7000	^{113}Cd, 100	10	
^{77}Se CP-CPMG	77	64	1000 5000 9000	^{77}Se, 83.3	10	
^{77}Se CP spin diffusion	77	64	9000	^{77}Se, 83.3 (π pulse), 2.5 (π/2 flip-back pulse)	10	
^{77}Se-^{77}Se refocused-INADEQUATE-CPMG	77	64	9000	^{77}Se, 83.3	10	
^{77}Se{^{113}Cd} 2D *J*-HMQC	56	61	9000	^{77}Se, 66.7 ^{113}Cd, 30.3	10	– 200
^{77}Se{^{113}Cd} *J*-HMQC curve	56	61	9000	^{77}Se, 66.7 ^{113}Cd, 2.5	10	– 55
	56	61	9000	^{77}Se, 66.7 ^{113}Cd, 2.5	10	– 320
	56	61	9000	^{77}Se, 66.7 ^{113}Cd, 30.3	10	– 200
^{77}Se{^{113}Cd} *J*-	56	61	9000	^{77}Se, 66.7	9.009	– 55

resolved curve				^{113}Cd, 2.3		
	56	61	9000	^{77}Se, 66.7 ^{113}Cd, 2.3	9.009	– 320
	56	61	9000	^{77}Se, 66.7 ^{113}Cd, 30.3	10	– 55
	56	61	9000	^{77}Se, 66.7 ^{113}Cd, 30.3	10	– 320
	56	61	9000	^{77}Se, 66.7 ^{113}Cd, 30.3	10	– 200
^{113}Cd{^{77}Se} *J*-resolved curve	51	25	8000	^{113}Cd, 30.3 ^{77}Se, 66.7	10	– 320

Table S2. NMR experimental parameters (recycle delays, number of scans, indirect dimension time-domain (TD) points, CPMG parameters, and experimental time)

Experiment	Recycle Delay (s)	# of Scans	Indirect Dimension TD Points	CPMG Parameters (Number of rotor cycles per half echo, CPMG loops)	Experimental Time (min)
CdSe nanoplatelets					
^{13}C CP spin echo (microwave Off)	5	128	-	-	11.5
^{13}C CP spin echo (microwave On)	5	128	-	-	11.5
^{113}Cd CP-CPMG (each)	15.6	32	-	6, 24	8.5
^{113}Cd CP pulse cooling	-	-	-	-	-
^{113}Cd-^{113}Cd CP-MAT	3.5	28	320	-	526
^{113}Cd-^{113}Cd refocused-INADEQUATE-CPMG	4.5	128	86	6, 24	840
^{77}Se CP-CPMG (each)	16.25	32	-	12, 16	9
^{77}Se CP spin diffusion	-	-	-	-	-
^{77}Se-^{77}Se refocused-INADEQUATE-CPMG	14	64	50	8, 26	751
^{77}Se{^{113}Cd} 2D *J*-HMQC	14	48	90	10, 22	1020
^{77}Se{^{113}Cd} *J*-HMQC curve (each)	15.6	80	20	6, 30	420
^{77}Se{^{113}Cd} *J*-resolved curve (each)	12	64	15	10, 20	194
^{113}Cd{^{77}Se} *J*-resolved curve	14.5	320	16	4, 48	1245
CdSe nanospheroids					
^{13}C CP spin echo (microwave Off)	6.4	32	-	-	3.5
^{13}C CP spin echo (microwave On)	6.4	32	-	-	3.5
^{113}Cd CP-CPMG (each)	6.4	64	-	6, 24	7
^{113}Cd CP pulse cooling	7	8	-	6, 24	22.5
^{113}Cd-^{113}Cd CP-MAT	3.25	28	280	-	427
^{113}Cd-^{113}Cd refocused-INADEQUATE-CPMG	3.25	128	70	6, 24	493
^{77}Se CP-CPMG	6.4	64	-	10, 18	7
^{77}Se CP spin diffusion	6.4	16	11	10, 18	800
^{77}Se-^{77}Se refocused-INADEQUATE-CPMG	6.4	128	50	5, 34	881

^{77}Se{^{113}Cd} 2D *J*-HMQC	11.2	32	84	4, 46	508
^{77}Se{^{113}Cd} *J*-HMQC curve (each)	11.2	64	20	2, 70	242
^{77}Se{^{113}Cd} *J*-resolved curve (each)	10	32	15	4, 46	81
^{113}Cd{^{77}Se} *J*-resolved curve	11.2	448	14	1, 120	1178

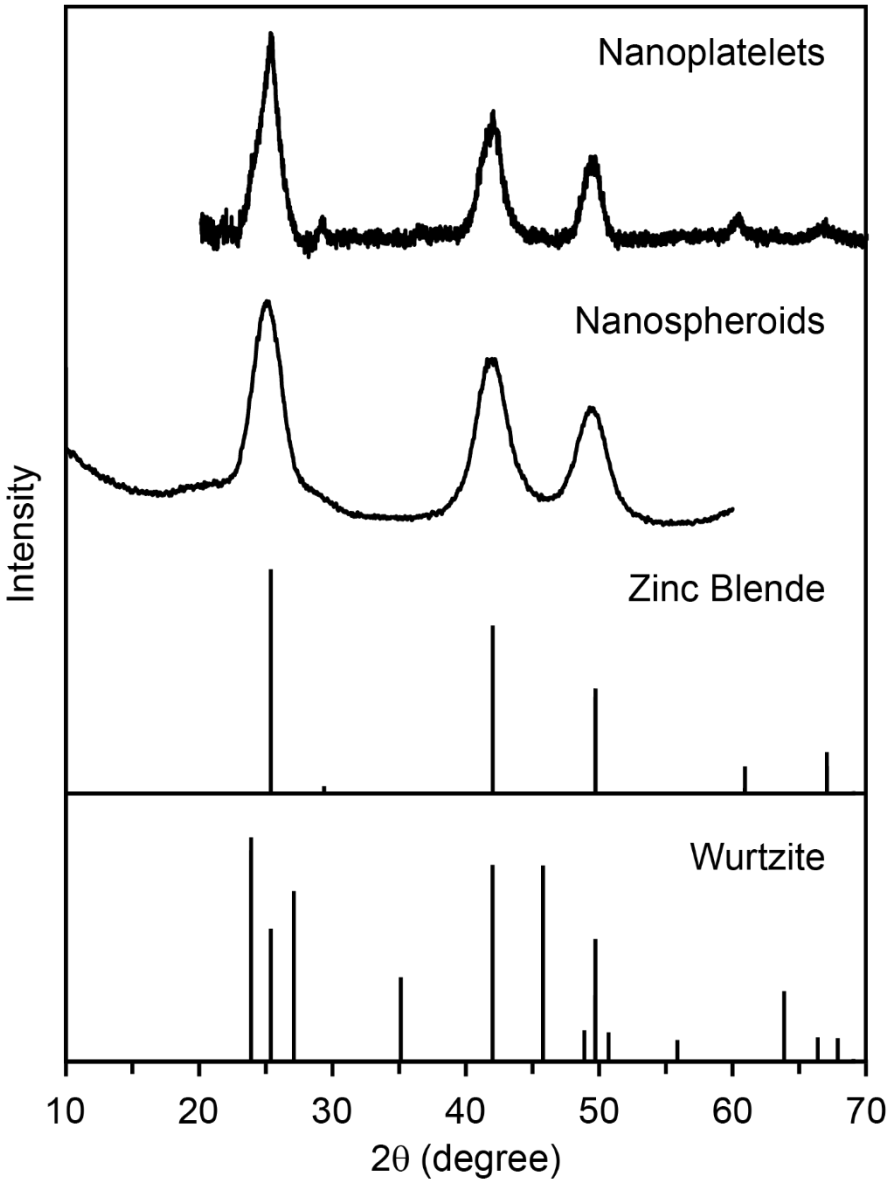

Figure S1. Powder XRD patterns of as synthesized CdSe nanoplatelets (Scherrer size: 6.4 ± 1.1 nm), CdSe nanospheroids (Scherrer size: 3.2 ± 0.2 nm), with Zinc Blende CdSe (ICSD #41528) and Wurtzite CdSe (ICSD #41491) shown for comparison.

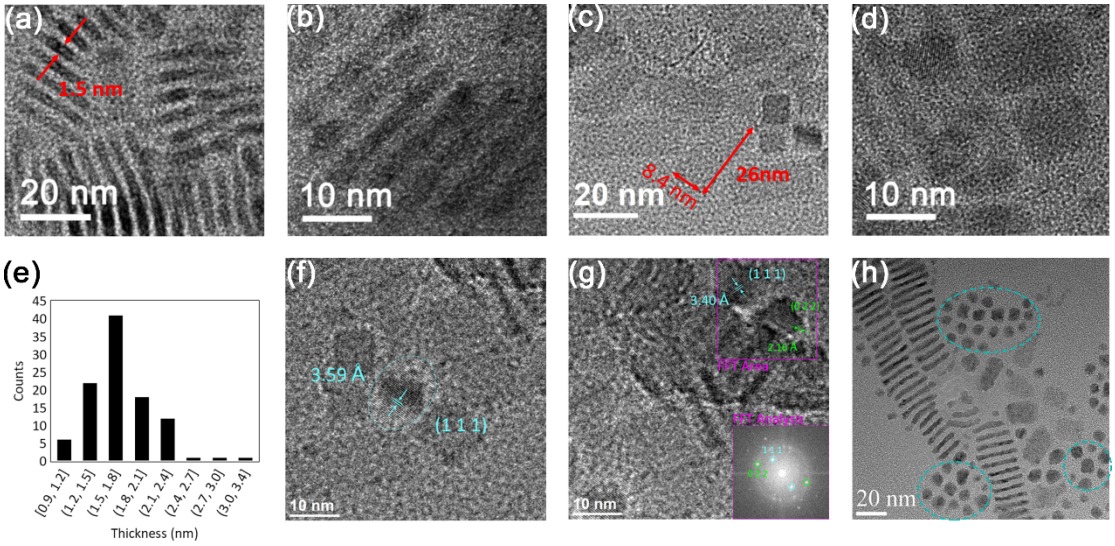

Figure S2. (a-d, h) Representative TEM images, (e) thickness histogram, and (f, g) HRTEM analysis of CdSe nanoplatelets. The thickness of nanoplatelets is 1.71 ± 0.40 nm and the average lateral dimensions are 8.4×26 nm^2. Lattice fringes of CdSe (111) and (022) are shown in the HRTEM. The blue circles with dotted lines in the TEM images of the nanoplatelets indicate spheroidal impurities.

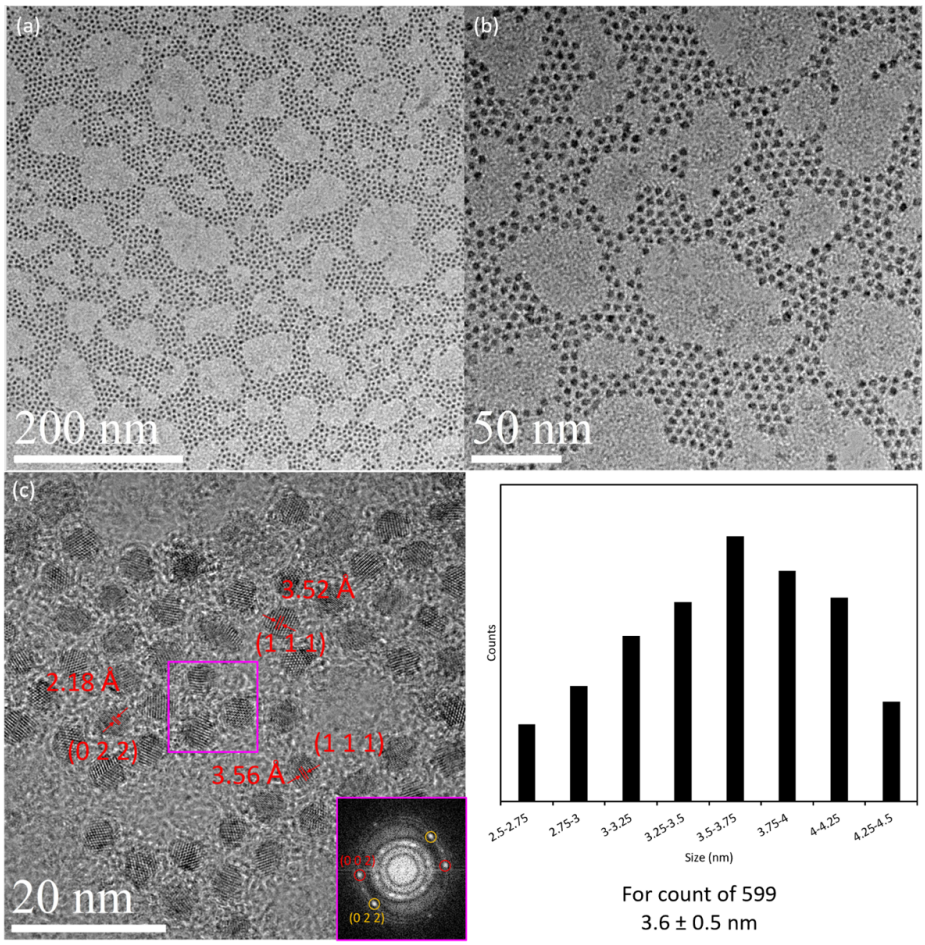

Figure S3. (a,b) Representative TEM images of CdSe nanospheroids, at lower magnification for visualization; (c) Lattice fringes of CdSe (111) and (022) are shown in the HRTEM obtained the inset in pink. The histogram was generated from (b) and shows a distribution of particle size: 3.6 ± 0.6 nm.

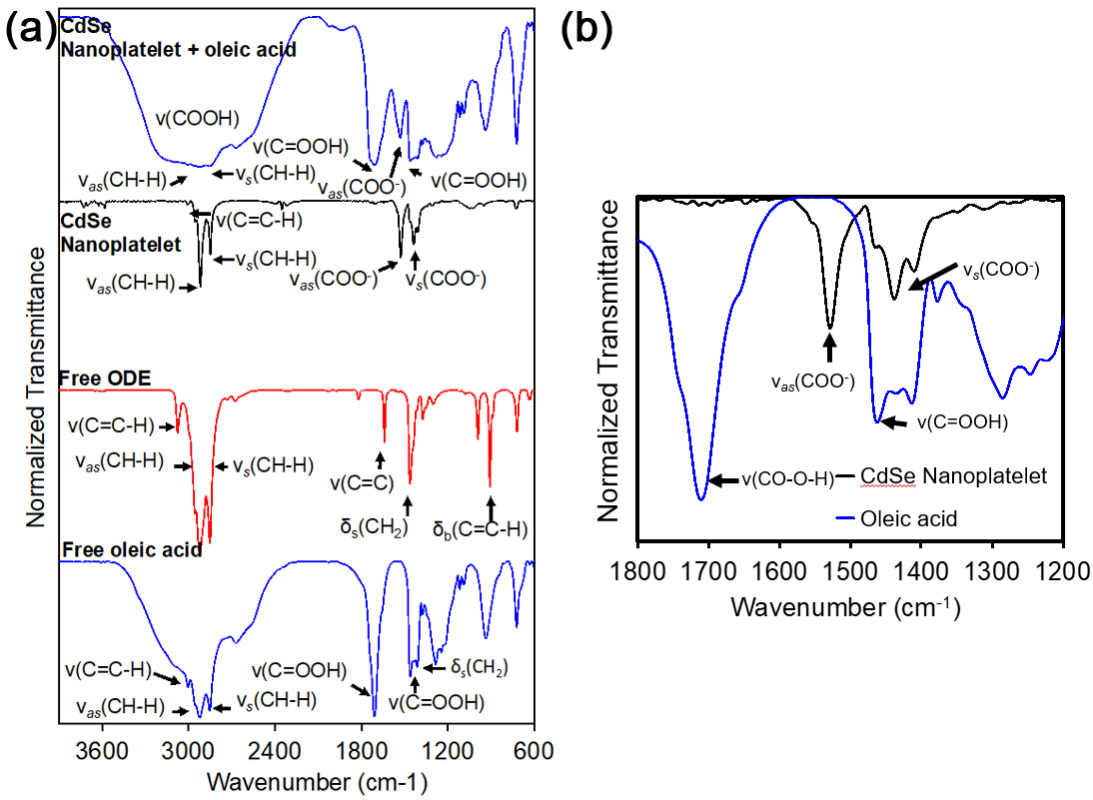

Figure S4. (a) IR spectra of CdSe nanoplatelets (blue, upper) with and (black) without oleic acid, (red) free ODE, and (blue, lower) free oleic acid; (b) comparison of CdSe nanoplatelets and free oleic acid in the 1200–1800 cm^{-1} range.

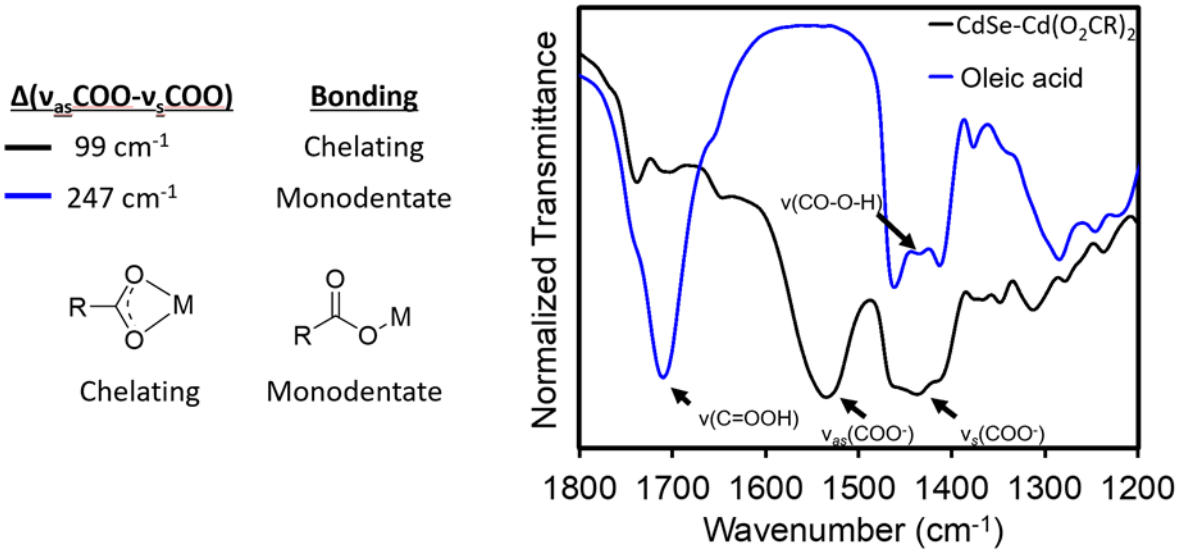

Figure S5. IR spectra of CdSe nanospheroids and free oleic acid. (Left) Chelating and monodentate bonding and the difference in their symmetric and asymmetric vibration modes. (Right) comparison of CdSe nanospheroids and free oleic acid in 1200–1800 cm^{-1} range.

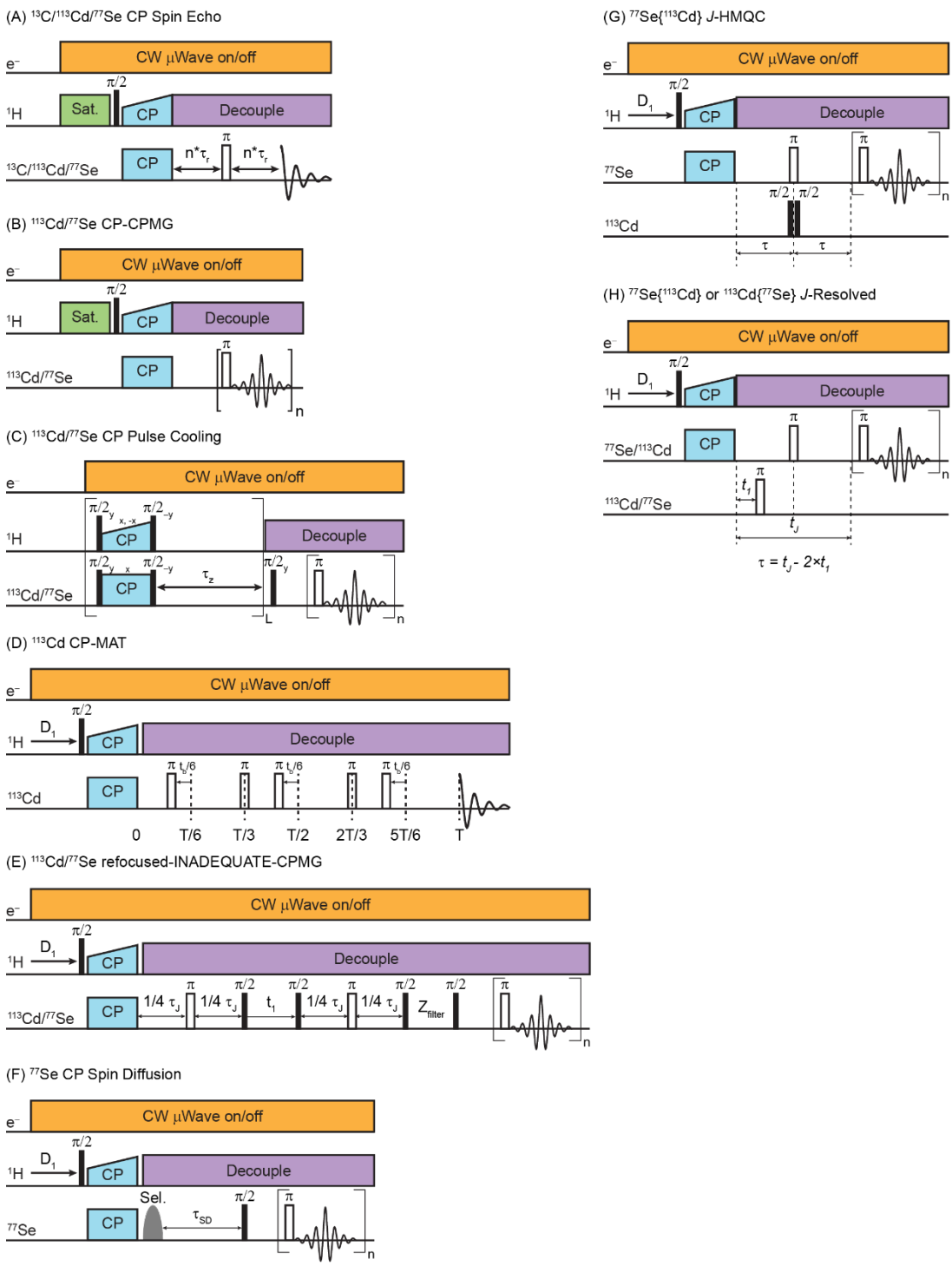

Figure S6. Pulse sequence diagrams for the different NMR experiments used in this work. (A) $^{13}C/^{113}Cd/^{77}Se$ CP spin echo, (B) $^{113}Cd/^{77}Se$ CP CPMG, (C) $^{113}Cd/^{77}Se$ CP pulse cooling, (D) ^{113}Cd CP-MAT, (E) $^{113}Cd/^{77}Se$ refocused-INADEQUATE-CPMG, (F) ^{77}Se CP spin diffusion, (G) $^{77}Se\{^{113}Cd\}$ *J*-HMQC and (H) $^{77}Se\{^{113}Cd\}$ or $^{113}Cd\{^{77}Se\}$ *J*-resolved experiments.

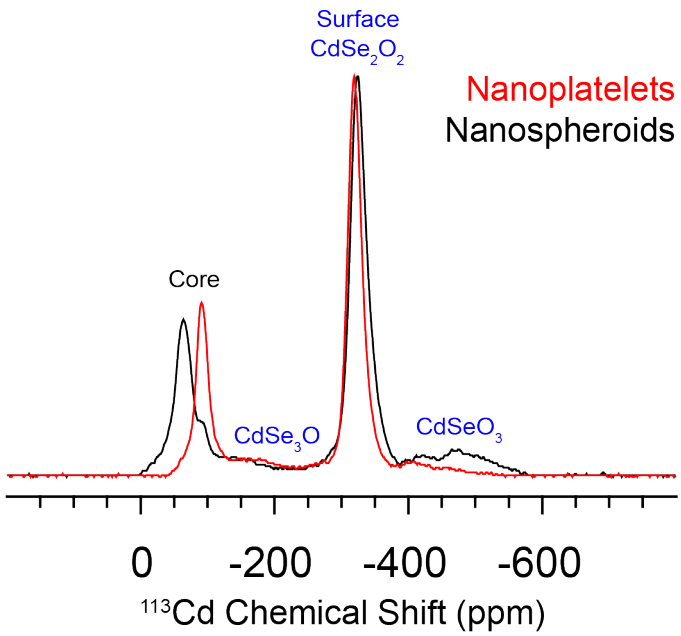

Figure S7. Comparisons of the positive projections of ^{113}Cd CP-MAT indirect dimensions.

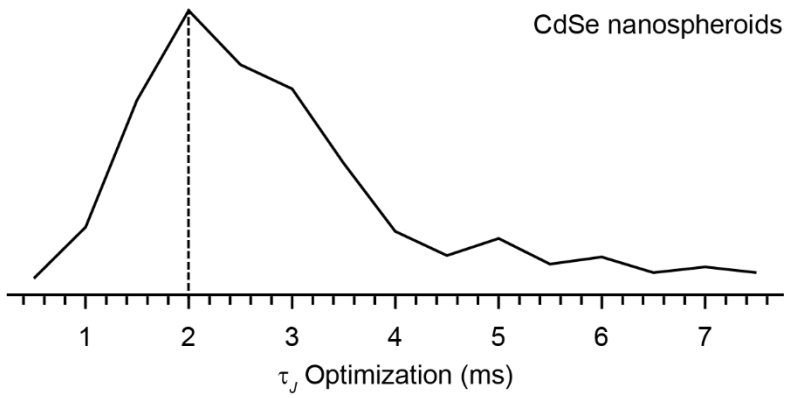

Figure S8. DNP-enhanced optimization of the scalar-coupling evolution time for ^{113}Cd-^{113}Cd refocused-INADEQUATE. The signal maximum at a mixing time of 2 ms suggests that the $^{2}J_{\text{Cd-Cd}} = 1/(4 \times 2\ \text{ms}) = 125$ Hz for the Cd atoms in the core of the CdSe NCs.

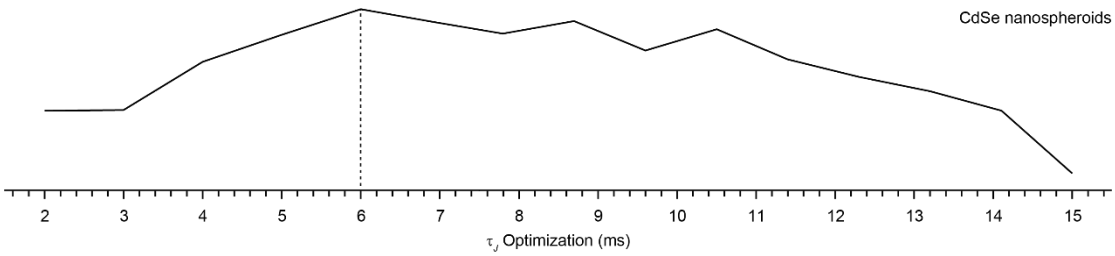

Figure S9. Optimization of the scalar-coupling evolution time for ^{77}Se-^{77}Se refocused-INADEQUATE. The signal maximum at a mixing time of 6 ms suggests that the $^{2}J_{\mathrm{Se-Se}} = 1/(4 \times 6\ \mathrm{ms}) \approx 42$ Hz Hz for the Se atoms in the core of the CdSe NCs.

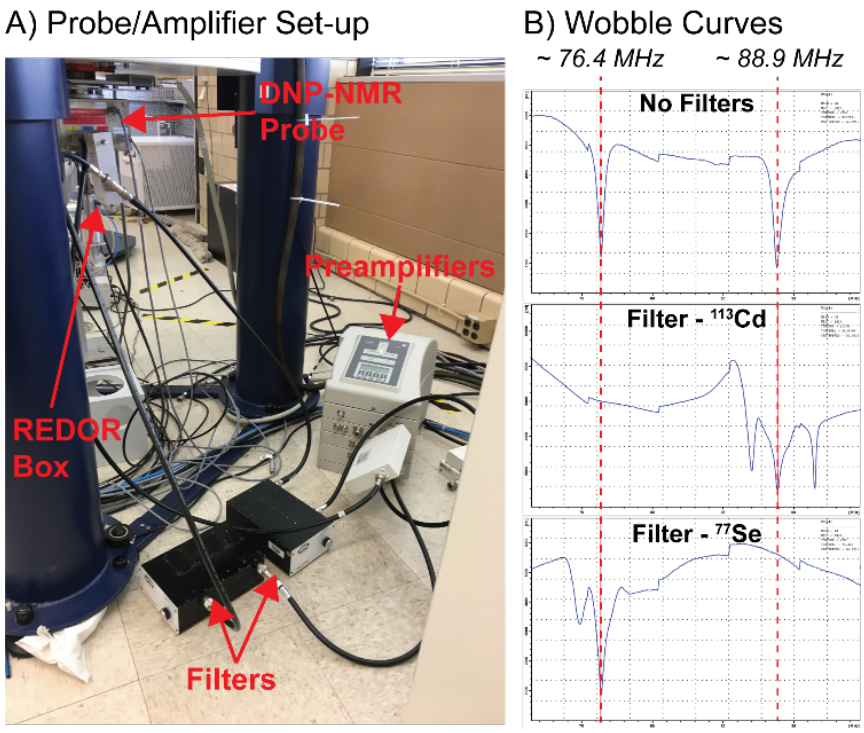

Figure S10. (A) DNP NMR probe/amplifier set-up used to enable ^{77}Se-^{113}Cd HETCOR experiments. In short, the DNP NMR probe was in double resonance configuration with a REDOR box RF frequency splitter connected to the X-channel to split the resonance frequency to both ^{77}Se and ^{113}Cd (B, upper). The X- and Y-preamplifiers were assigned to ^{77}Se and ^{113}Cd, respectively, and connected to the REDOR box through a T-joint. Adjustable RF filters were placed in between the preamplifiers and the REDOR box to isolate both channels (B, lower two).

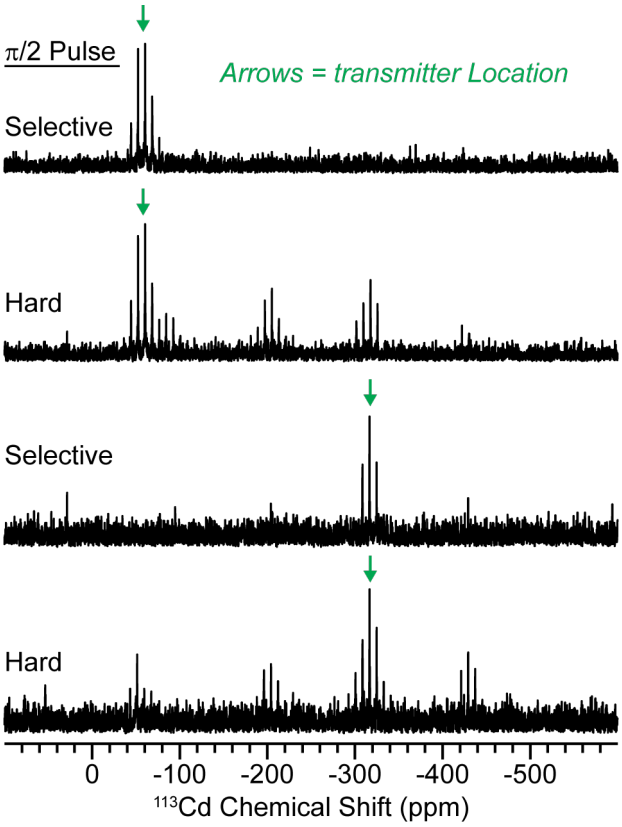

Figure S11. Comparison of $^{1}H \rightarrow ^{113}Cd$ CP flip-back spectra [$^{1}H \rightarrow ^{113}Cd$ CP – ^{113}Cd hard π/2 flip back – z-filter – hard or soft π/2 pulse to read the magnetization] of CdSe nanoplatelets with either hard (7.25 μs) or selective (100 μs) π/2 read pulses and the ^{113}Cd transmitter on resonance with the core ^{113}Cd signal (~ – 55 ppm) or surface ^{113}Cd signal (~ – 320 ppm); the green arrow denotes the location of the ^{113}Cd transmitter.

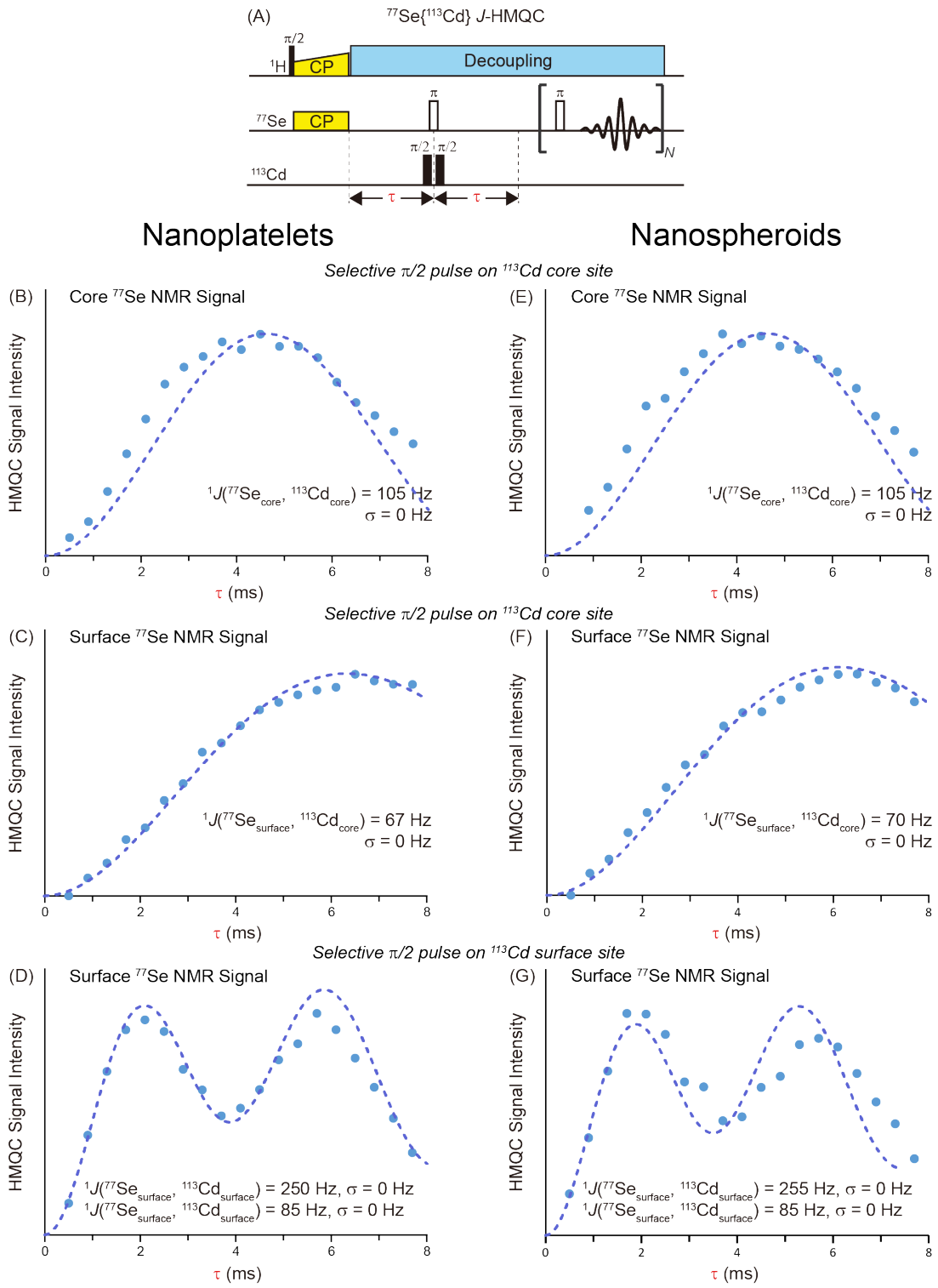

Figure S12. Fits for ^{77}Se{^{113}Cd} *J*-HMQC signal intensity build-up with single values of $^{1}J_{\text{Se-Cd}}$. (A) ^{77}Se{^{113}Cd} *J*-HMQC pulse program with variable ^{77}Se-^{113}Cd *J*-evolution periods (τ) on ^{113}Cd and ^{77}Se CPMG signal detection. The ^{113}Cd π/2 pulses were 100 μs in duration (2.5 kHz RF field) to allow selective excitation of surface or core Cd signals. (B–G) ^{77}Se{^{113}Cd} HMQC signal intensity as a function of τ for (B-D) CdSe nanoplatelets (B–D) and nanospheroids (E–G). (B, E) Selective π/2 pulses on ^{113}Cd core site, monitoring ^{77}Se core signal intensity. (C, F) Selective π/2 pulses on ^{113}Cd core

site, monitoring ^{77}Se surface signal intensity. (D, G) Selective π/2 pulses on ^{113}Cd surface site, monitoring ^{77}Se surface signal intensity. The purple dashed lines are the single value fit. The single value fit *J*-couplings are indicated on the plots.

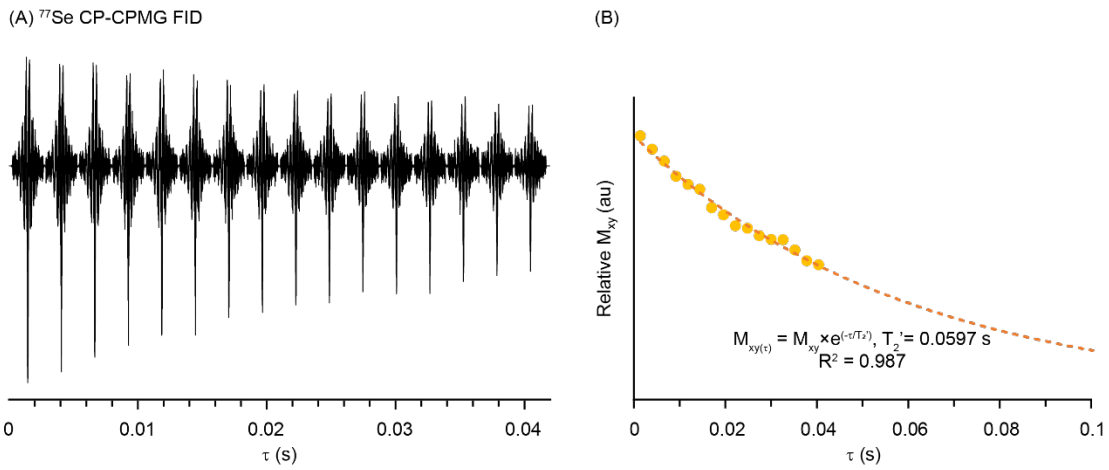

Figure S13. (A) ^{77}Se CP-CPMG FID and (B) Graph of the relative intensity of the transverse magnetization *versus* total evolution time (τ). The orange dashed line is the best fit for T_2'. The best-fit T_2' is indicated on the plot. A T_2' of 60 ms was measured from the decay of the echo amplitudes in the CPMG train. This T_2' was used when fitting the intensity of ^{77}Se{^{113}Cd} J-HMQC core Se NMR signals. However, a T_2' of 20 ms was used for fitting build-up of ^{77}Se{^{113}Cd} J-HMQC surface Se NMR signals because CPMG is known to overestimate the measured transverse relaxation time due to contributions from stimulated echo pathways. The shorter value of T_2' for the surface Se NMR signals was required to obtain an equal probability (amplitude of strong and weak J-couplings).

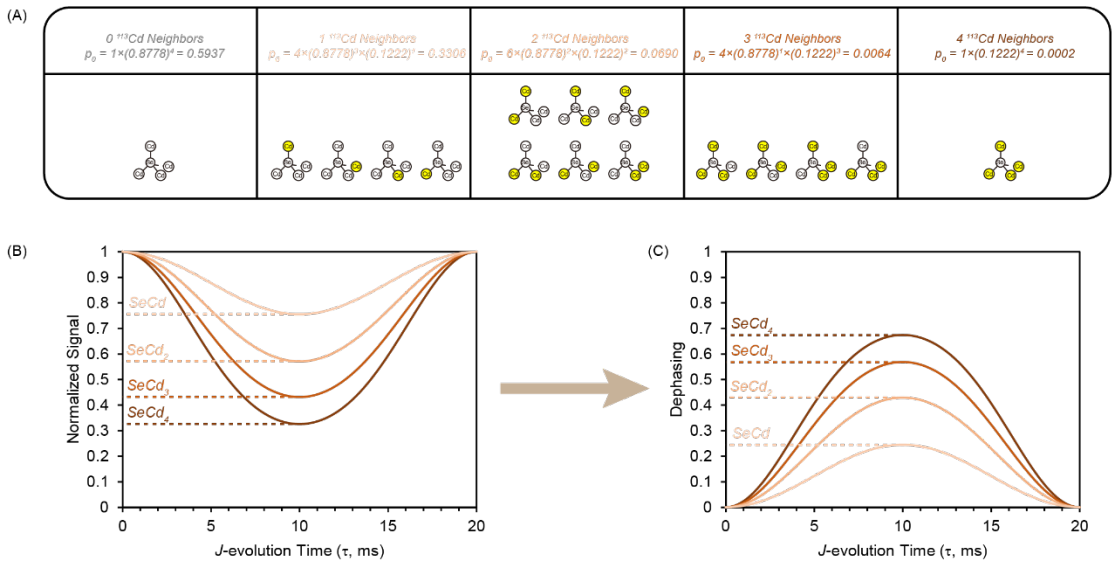

Figure S14. The dependence of the extent of dephasing observed in a ^{77}Se{^{113}Cd} *J*-resolved NMR experiments on the SeCd$_n$ stoichiometry. (A) For a tetrahedral SeCd$_4$ site the probabilities of having isotopomers with 0, 1, 2, 3, and 4 attached ^{113}Cd spins is $p_0 = 0.5937$, $p_1 = 0.3306$, $p_2 = 0.0690$, $p_3 = 0.0064$ and $p_4 = 0.0002$, respectively. (B) Analytical simulation of the normalized signal intensity *versus* *J*-evolution time for SeCd$_4$, SeCd$_3$, SeCd$_2$ and SeCd with $^1J_{\text{Se-Cd}}$ = 100 Hz. (C) Graph of the extent of dephasing *versus* *J*-evolution time (τ), where dephasing = 1 – Normalized Signal. The text below gives the calculation of the probabilities for SeCd$_3$, SeCd$_2$ and SeCd fragments.

Table S3. Probabilities of isotopomers with different numbers of attached ^{113}Cd spins for different SeCd$_3$, SeCd$_2$ and SeCd units.

Coordination	p_0	p_1	p_2	p_3
SeCd$_3$	$(0.8778)^3$ = 0.676	3×(0.1222)× $(0.8778)^2$ = 0.282	3×$(0.1222)^2$× (0.8778) = 0.0393	$(0.1222)^3$ =0.0018
SeCd$_2$	$(0.8778)^2$ = 0.771	2×(0.1222)× (0.8778) = 0.215	$(0.1222)^2$ = 0.015	
SeCd	0.8778	0.1222		

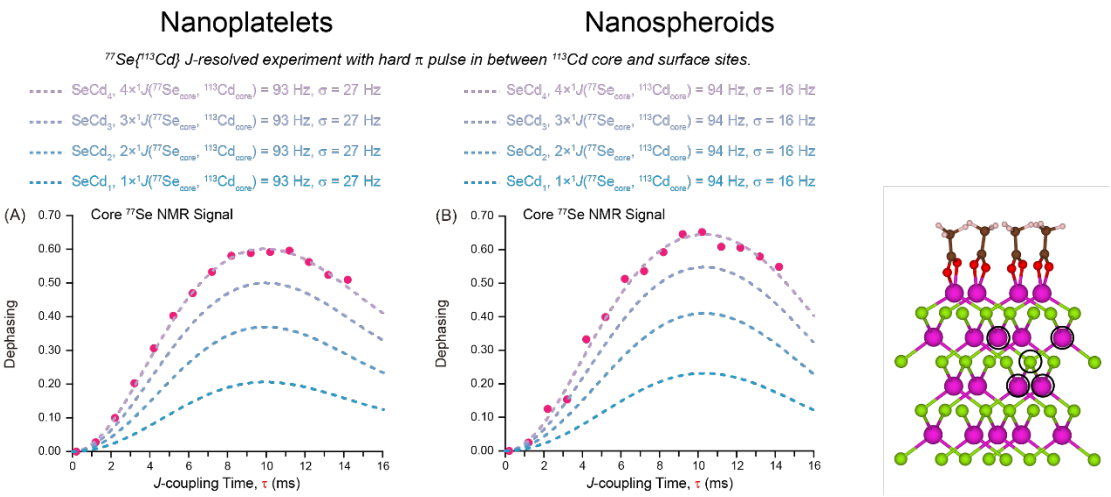

Figure S15. Analytical simulations of signal dephasing of SeCd, $SeCd_2$, $SeCd_3$ and $SeCd_4$ coordination for $^{77}Se\{^{113}Cd\}$ *J*-resolved experiments. (A, B) Dependence of the ^{77}Se signal dephasing on the *J*-coupling evolution time (τ) for CdSe nanoplatelets (A) and nanospheroids (B) in $^{77}Se\{^{113}Cd\}$ *J*-resolved experiments (pink dots) with a hard π pulse in between ^{113}Cd core and surface sites, monitoring ^{77}Se core signal dephasing. The SeCd, $SeCd_2$, $SeCd_3$ and $SeCd_4$ coordination fit *J*-couplings are indicated on the plots.

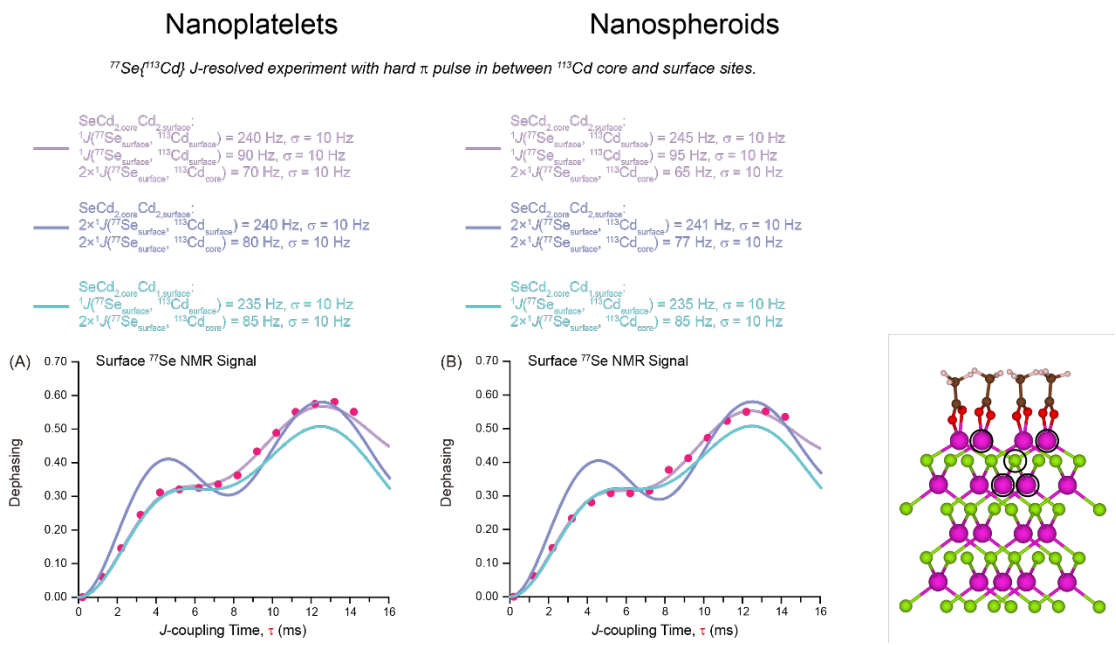

Figure S16. Analytical simulations of signal dephasing of $SeCd_{2,core}Cd_{2,surface}$ and $SeCd_{2,core}Cd_{1,surface}$ coordination for $^{77}Se\{^{113}Cd\}$ *J*-resolved experiments. (A, B) Dependence of the ^{77}Se signal dephasing on the *J*-coupling evolution time (τ) for CdSe nanoplatelets (A) and nanospheroids (B) in $^{77}Se\{^{113}Cd\}$ *J*-resolved experiments (pink dots) with a hard π pulse in between ^{113}Cd core and surface sites, monitoring ^{77}Se surface signal dephasing. The $SeCd_{2,core}Cd_{2,surface}$ and $SeCd_{2,core}Cd_{1,surface}$ coordination fit *J*-couplings are indicated on the plots. Note that $SeCd_{2,core}Cd_{2,surface}$ coordination has two sets of *J*-couplings fit: (240 Hz, 90 Hz, 70 Hz, 70 Hz) and (240 Hz, 240 Hz, 80 Hz, 80 Hz).

Supporting Information References:

(1) Grabolle, M.; Spieles, M.; Lesnyak, V.; Gaponik, N.; Eychmüller, A.; Resch-Genger, U., Determination of the Fluorescence Quantum Yield of Quantum Dots: Suitable Procedures and Achievable Uncertainties. *Anal. Chem.* **2009,** *81* (15), 6285-6294.